ACS NANO
Cite This: ACS Nano 2018, 12, 9162–9176
www.acsnano.org

ARTICLE

High F-Content Perfluoropolyether-Based Nanoparticles for Targeted Detection of Breast Cancer by ^{19}F Magnetic Resonance and Optical Imaging

Cheng Zhang,[†,‡] Shehzahdi Shebbrin Moonshi,[†,‡] Wenqian Wang,[§,∥] Hang Thu Ta,[†] Yanxiao Han,[⊥] Felicity Y. Han,[○] Hui Peng,[†,‡] Petr Král,[⊥,#,▽] Barbara E. Rolfe,[†] John Justin Gooding,[§,∥,◆] Katharina Gaus,[§,¶,+] and Andrew Keith Whittaker*[,†,‡]

[†]Australian Institute for Bioengineering and Nanotechnology and [‡]ARC Centre of Excellence in Convergent Bio-Nano Science and Technology, The University of Queensland, Brisbane, Qld 4072, Australia

[§]Australian Centre for NanoMedicine and [∥]School of Chemistry, University of New South Wales, Sydney 2052, Australia

[⊥]Department of Chemistry and [#]Department of Physics, University of Illinois at Chicago, Chicago, Illinois 60607, United States

[▽]Department of Biopharmaceutical Sciences, University of Illinois at Chicago, Chicago, Illinois 60612, United States

[○]Centre for Integrated Preclinical Drug Development, The University of Queensland, Brisbane, Qld 4072, Australia

[◆]ARC Centre of Excellence in Convergent Bio-Nano Science and Technology, [¶]EMBL Australia Node in Single Molecule Science, and [+]ARC Centre of Excellence in Advanced Molecular Imaging, University of New South Wales, Sydney 2052, Australia

Supporting Information

ABSTRACT: **Two important challenges in the field of ^{19}F magnetic resonance imaging (MRI) are the maintenance of high fluorine content without compromising imaging performance, and effective targeting of small particles to diseased tissue. To address these challenges, we have developed a series of perfluoropolyether (PFPE)-based hyperbranched (HBPFPE) nanoparticles with attached peptide aptamer as targeting ligands for specific *in vivo* detection of breast cancer with high ^{19}F MRI sensitivity. A detailed comparison of the HBPFPE nanoparticles (NPs) with the previously reported trifluoroethyl acrylate (TFEA)-based polymers demonstrates that the mobility of fluorinated segments of the HBPFPE nanoparticles is significantly enhanced (^{19}F T_2 > 80 ms vs 31 ms), resulting in superior MR imaging sensitivity. Selective targeting was confirmed by auto- and pair correlation analysis of fluorescence microscopy data, *in vitro* immunofluorescence, *in vivo* ^{19}F MRI, *ex vivo* fluorescence and ^{19}F NMR. The results highlight the high efficiency of aptamers for targeting and the excellent sensitivity of the PFPE moieties for ^{19}F MRI. Of relevance to *in vivo* applications, the PFPE-based polymers exhibit much faster clearance from the body than the previously introduced perfluorocarbon emulsions ($t_{1/2}$ ∼ 20 h vs up to months). Moreover, the aptamer-conjugated NPs show significantly higher tumor-penetration, demonstrating the potential of these imaging agents for therapeutic applications. This report of the synthesis of polymeric aptamer-conjugated PFPE-based ^{19}F MRI CAs with high fluorine content (∼10 wt %) demonstrates that these NPs are exciting candidates for detecting diseases with high imaging sensitivity.**

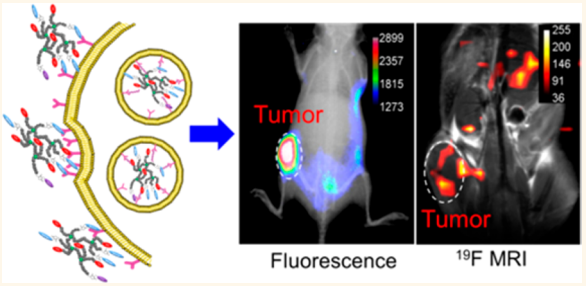

KEYWORDS: *^{19}F magnetic resonance imaging, breast cancer, perfluoropolyether-based nanoparticles, in vivo bioimaging, aptamers*

Over the past several decades ^{19}F magnetic resonance imaging (MRI) has been demonstrated to have enormous potential for applications in molecular imaging, including for cell tracking, sensing of oxygen partial pressure, and detection of disease.[1−4] The ^{19}F nucleus has 100% natural abundance and its gyromagnetic ratio (40.06 MHz/T) is approaching that of protons, and thus, MRI of fluorine is potentially more sensitive than for other nuclei. Importantly, the absence of endogenous ^{19}F MR signal in the body, and the reported linear relationship between fluorine

Received: May 17, 2018
Accepted: August 17, 2018
Published: August 17, 2018

DOI: 10.1021/acsnano.8b03726
ACS Nano 2018, 12, 9162–9176

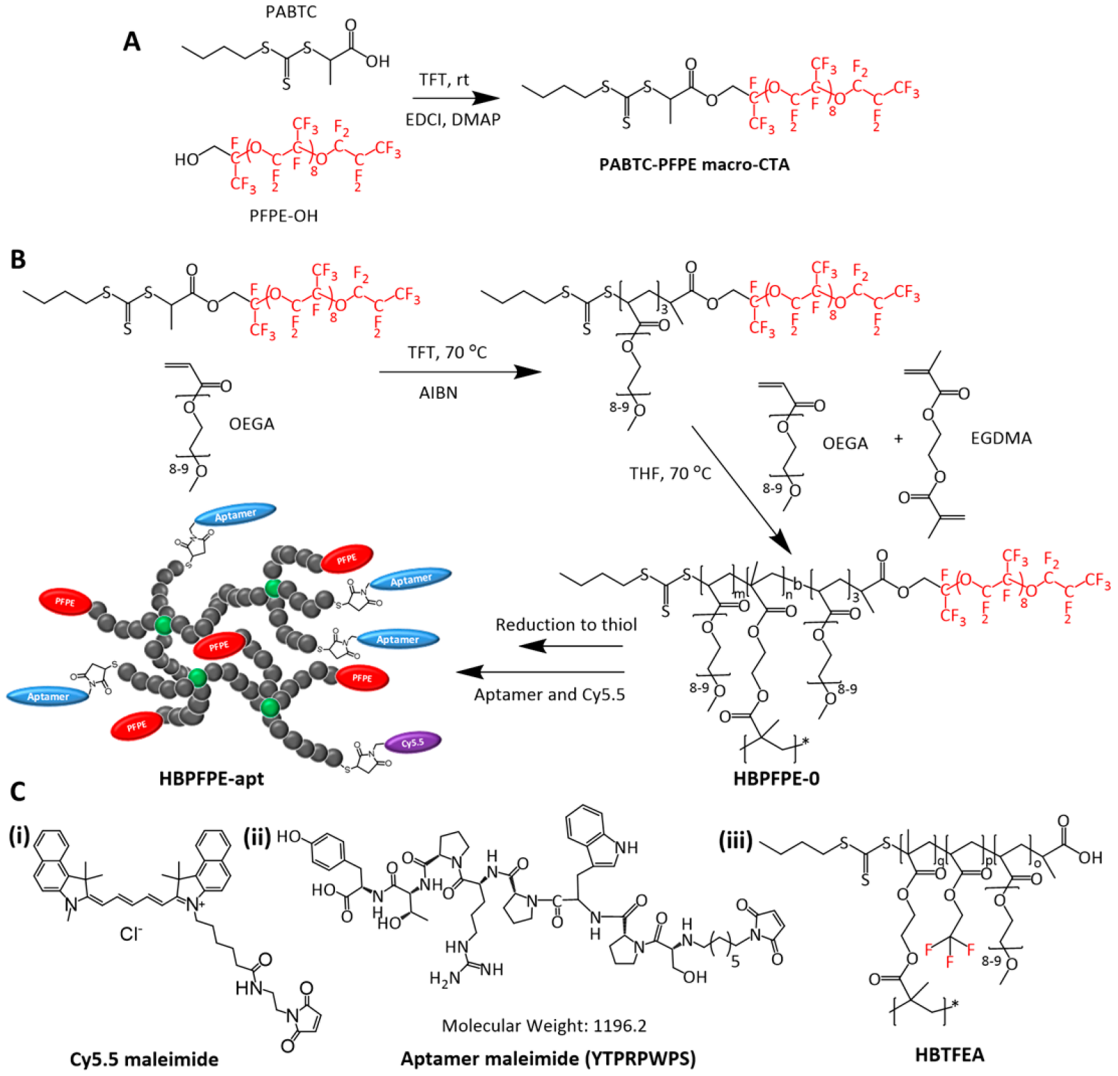

Figure 1. Synthetic routes for preparation of the PABTC-PFPE macro-CTA and hyperbranched PFPE-based nanoparticles. (A) EDCI/DMAP esterification between PABTC and PFPE-OH was performed in trifluorotoluene (TFT). (B) Homopolymerization of OEGA was conducted in the presence of PABTC-PFPE macro-RAFT agent. Chain extension was performed to obtain the polymer HBPFPE-0. The conjugation of fluorescence dye molecules (Cy5.5) and targeting ligands (peptide aptamer) was then performed using thiol-maleimide "click" reactions. The HBPFPE nanoparticles without and with conjugation of aptamer are denoted as HBPFPE-non and HBPFPE-apt, respectively. (C) Chemical structures of the Cy5.5 fluorescence dye, peptide aptamer, and the hyperbranched 2,2,2-trifluoroethyl acrylate-based (HBTFEA) polymer.[20,21]

concentration and resulting MRI signal intensity means that quantitative imaging experiments can be conducted.[5−7] Measurement of the number of imaging agent molecules or particles within a particular imaging volume element is often highly challenging for imaging agents based on paramagnetic ions or particles.

Despite these manifest advantages, ^{19}F MRI is less clinically relevant than ^{1}H MRI.[8,9] This is in part due to the requirement of a high local fluorine concentration within the imaging volume while maintaining high segmental mobility of the fluorine-containing moieties of the fluorinated compounds. A number of highly fluorinated molecules, such as perfluorinated crown ethers (PFCE), perfluoropolyethers (PFPE)[10,11] or highly fluorinated small molecules[12] have been introduced to overcome these limitations. Emulsions of such highly fluorinated molecules are the current state-of-the-art ^{19}F MRI contrast agents (CAs) for preclinical and/or clinical studies, however they have some limitations. For example, these emulsions are often poorly stable particularly in blood and have long retention times in the body of up to months.

In response, researchers are actively examining fluorinated polymers as alternative ^{19}F MRI agents.[13−17] Polymeric species have properties of high stability, controllable physicochemical properties, relatively simple synthesis and, when appropriately designed, are cleared rapidly from the body. However, a major limitation of fluorinated polymers as effective ^{19}F MRI agents is their low fluorine content (normally <5 wt %), which leads to low sensitivity as compared to fluoro-emulsions.[18−25] Therefore, the application of polymeric ^{19}F MR imaging agents for *in vivo* studies is rarely reported and most studies have focused on the design and structural optimization of the fluorinated polymers. For example, Guo et al. in 2016 reported a fluorinated branched polyethylenimine (PEI) prepared using ethyl trifluoroacetate (TFAET) as the fluorinated segment and lactobionic acid (LA) as the targeting ligand (PEI-LA-CF_3, fluorine content: ∼10 wt %).[26] *In vivo* experiments were

DOI: 10.1021/acsnano.8b03726
ACS Nano 2018, 12, 9162−9176

successfully conducted, and a good signal-to-noise ratio (SNR) in ^{19}F MRI was achieved after a high-dose intravenous injection of 30 mg of PEI-LA-CF_3. However, concerns must be raised over the safety of administration of PEI-based polymers to the body at such a high dose, despite the authors having argued that the charge density was largely minimized after conjugation of TFAET and LA. In order to reduce the injection dose of fluorinated imaging agents to lower the health risks, perfluoropolyether-based nanoparticles have been developed in our group with higher fluorine content (up to ~30 wt %) and long ^{19}F NMR spin−spin T_2 relaxation times (>80 ms in serum) to ensure high *in vivo* ^{19}F MRI sensitivity. Furthermore, the injection dose could be reduced to 4 mg of polymer per mouse (body mass ~18 g) while maintaining excellent *in vivo* ^{19}F MR imaging sensitivity.[27,28] The polymers introduced in this current report differ from the previously studied linear copolymers by having a highly branched architecture and consequent higher content of PFPE end groups. Such branched architecture is important for biomedical applications to provide multiple functionalities for attachment of both targeting ligands and complementary imaging modalities on a single molecule.

Active and specific targeting of diseased tissues is essential for diagnostic imaging and for delivery of therapy to the site of disease. Peptide aptamers are promising recognition units that can not only specifically bind to target molecules and cells, but also have demonstrated superior tumor penetration compared with other targeting ligands, such as full antibodies.[29,30] Due to their relative small size, low immunogenicity, excellent specificity, and high affinity to targets, peptide aptamers have attracted attention in various fields in which selective recognition units are required. The simple and readily accessible procedures for synthesis for peptide aptamers is another advantage, thus facilitating facile conjugation to molecular imaging probes or carriers.[31,32]

Breast cancer is one of the leading causes of cancer-related deaths in women worldwide with increasing incidence in developing countries.[33] It has been widely reported that breast tumor cells overexpress heat shock proteins which play a pivotal role in breast tumor development owing to their intrinsic molecular chaperone properties.[34] Rérole and co-workers have recently demonstrated the synthesis of peptide aptamers with high affinity for this class of surface-presenting proteins.[35] Peptide aptamers can be readily modified with other functional groups, such as imaging modalities and therapeutic segments, and thus have great potential as effective platforms for specific detection and treatment of breast cancer.

In this report, we describe the design of multifunctional PFPE-based nanoparticles conjugated with a peptide aptamer as targeting ligand. The aptamer-conjugated PFPE-based nanoparticles can not only specifically target the heat shock protein 70 (Hsp70) overexpressed in breast cancer cells with high selectivity, but have high tumor penetration and can be rapidly cleared from the body. Our results suggest that the PFPEs are promising candidates for the preparation of sensitive partially fluorinated polymers as ^{19}F MRI CAs and demonstrate an exciting direction for the preparation of next-generation ^{19}F MRI CAs.

RESULTS AND DISCUSSION

Synthesis and Characterization of Hyperbranched Perfluoropolyether-Based (HBPFPE) Nanoparticles. In this report we describe the synthesis and evaluation of highly sensitive ^{19}F MRI contrast agents for the detection of breast cancer *in vivo*. Hyperbranched perfluoropolyether-based (HBPFPE) nanoparticles (NPs) conjugated with targeting aptamers were prepared by reversible addition−fragmentation chain transfer (RAFT) polymerization. The use of RAFT chemistry imparts several advantages: all arms of the hyperbranched polymers have well-defined end-groups which can be further functionalized with targeting ligands, fluorescent chromophores or therapeutic drugs. The HBPFPE nanoparticles consist of hydrophobic PFPE segments to provide an intense ^{19}F MRI signal and oligo(ethylene glycol) methyl ether acrylate (OEGA) as the hydrophilic monomer to enhance aqueous solubility. After polymerization, the RAFT agent thiocarbonylthio groups residing at the termini of the chains were reduced to thiols to allow conjugation of Cy5.5 dye and an appropriate aptamer peptide, to enable *in vivo* optical imaging, determination of polymer biodistribution and ensure specific recognition of breast cancer cells.

As illustrated in Figure 1A, a polymerizable macro-chain-transfer agent (macro-CTA) was first prepared following previously reported procedures.[27] The esterification reaction between (propionic acid)yl butyl trithiocarbonate (PABTC) and monohydroxy PFPE was conducted using the standard dicyclohexylcarbodiimide/4-dimethylaminopyridine (EDCI/DMAP) coupling method. ^{1}H and ^{19}F NMR spectra of PABTC, monohydroxy PFPE and macro-CTA in $CDCl_3$ and the assignments to the spectra were shown in Figure S1 and S2, indicating the successful synthesis of the PABTC-PFPE macro-CTA.

Homopolymers of OEGA with PFPE as terminal units (poly$(OEGA)_3$-PFPE, $M_{n,NMR}$ = 3100 g/mol, D_M = 1.06) were prepared through RAFT polymerization. The extent of conversion of OEGA monomer to polymer was ~89%, as determined from the integrated intensities of appropriate peaks in the ^{1}H NMR spectrum of the crude sample (Figure S3). The poly$(OEGA)_3$-PFPE polymer was then used as a polymeric macro-CTA and further chain extended with OEGA and ethylene glycol dimethyl acrylate (EGDMA) monomers resulting in a hyperbranched PFPE-based polymer with multiple functional chain ends in one molecule (HBPFPE-0, Figure 1B). Confirmation of the successful synthesis of the HBPFPE polymer was obtained via determination of the absolute molecular weight of the polymers using multiangle laser light scattering (MALLS) and size exclusion chromatography (SEC). The number of chain ends on the hyperbranched polymers were also calculated by comparing the molar mass for each arm determined by ^{1}H NMR with the absolute molar mass determined from light scattering by GPC-MALLS. The results are listed in Table S1.[21,36]

In the next step, the terminal trithiocarbonate groups of the HBPFPE polymer were reduced to thiol groups in the presence of hexylamine to allow attachment of fluorophores and/or targeting ligands to the periphery of HBPFPE nanoparticles through thiol-maleimide "click" chemistry. The fluorophore used here was the Cy5.5 fluorescence dye with a maleimide functional group (Ex/Em: 684/710 nm) to allow *in vitro*, *in vivo*, and *ex vivo* tracking of the polymer (Figure 1Ci). The targeting ligand was a peptide aptamer (Figures 1Cii and S4, sequence: SPWPRPTY) with the N-terminus modified with a maleimide group to allow attachment to the HBPFPE polymer by "click" chemistry. The HBPFPE nanoparticles (unconjugated and conjugated with aptamer) are denoted as

DOI: 10.1021/acsnano.8b03726
ACS Nano 2018, 12, 9162−9176

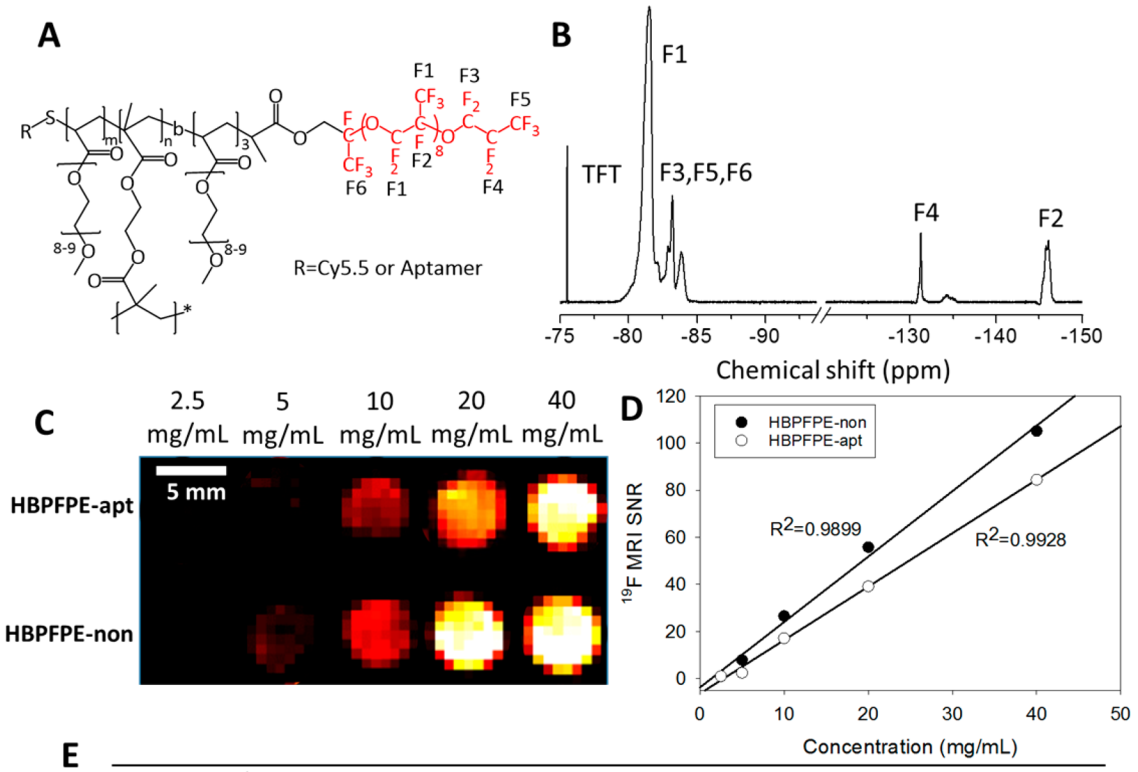

E

Concentration (mg/mL)	HBPFPE-non		HBPFPE-apt	
	^{19}F NMR T_1 (ms)	^{19}F NMR T_2 (ms)	^{19}F NMR T_1 (ms)	^{19}F NMR T_2 (ms)
2.5	371.1±5.6	82.9±2.2	384.6±7.5	84.2±1.3
5	376.5±7.1	87.6±3.4	380.2±5.8	85.3±3.2
10	386.3±5.8	85.5±1.4	377.6±5.5	84.5±2.4
20	378.6±3.3	84.0±3.1	384.3±6.3.	86.4±1.1
40	382.5±5.1	86.6±3.2	369.5±7.6	88.5±2.6

Figure 2. ^{19}F NMR and MRI properties of the HBPFPE nanoparticles at a magnetic field of 9.4 T. (A) Chemical structure of the HBPFPE nanoparticles (HBPFPE-non: Cy5.5-conjugated. HBPFPE-apt: Cy5.5- and aptamer-conjugated). (B) Typical ^{19}F NMR spectrum of HBPFPE-apt in PBS in the presence of 10% of FBS and assignment to the spectrum. (C) ^{19}F MRI images of solutions of HBPFPE-non and HBPFPE-apt at a range of sample concentrations. (D) ^{19}F MRI signal-to-noise ratio (SNR) of HBPFPE-non and HBPFPE-apt increases linearly with respect to concentration, indicating no concentration dependent aggregation. (E) ^{19}F NMR relaxation times measured for peak F1 for HBPFPE-non and HBPFPE-apt showing no appreciable change as a function of concentration. The table in part E of the figure reports the mean ± standard deviation (SD, n = 3).

HBPFPE-non and HBPFPE-apt, respectively. The peptide aptamer has been shown to have high specificity for binding to heat shock protein 70 (Hsp70), which is overexpressed in many tumors.[35] The successful conjugation of the aptamer was confirmed from the ^{1}H NMR spectrum in which the characteristic peaks of the aptamer located at >6.5 ppm are observed (Figure S5). The number of aptamers conjugated to the polymer was calculated by comparison of the integrals of peaks due to the methylene protons (2H) adjacent to the ester groups from OEGA and the hydroxyl group (1H) next to the benzene ring from the aptamer. Such calculations indicate that one HBPFPE-apt polymer has approximate three aptamers attached. The conjugation efficiency of Cy5.5 fluorescence dye was determined to be 0.75 and 0.55 wt % for HBPFPE-non and HBPFPE-apt, respectively (Figure S6). The observation of sharp and intense peaks in the ^{19}F NMR spectra of both polymers (Figure S7) confirms there were no large-scale changes in segmental dynamics of the molecule on attachment of the peptide aptamer and dye. Moreover, we have confirmed that the HBPFPE polymers are unimers by comparing the hydrodynamic sizes in $CHCl_3$ and under biological conditions (9.5 and 10.1 nm in $CHCl_3$ compared to 6.5 and 7.8 nm in the presence of FBS in PBS for HBPFPE-non and HBPFPE-apt, respectively).

In order to be effective as a ^{19}F MRI agent, the fluorine content of the polymer must be high and the fluorinated segments must maintain large-amplitude segmental mobility in order to achieve long transverse relaxation times (^{19}F NMR T_2 relaxation times) required by spin echo or gradient echo MRI pulse sequences. Therefore, the ^{19}F NMR properties of the HBPFPE NPs were examined to confirm the suitability of these polymers as ^{19}F MRI contrast agents. Sharp and intense peaks can be observed in the ^{19}F NMR spectra of the HBPFPE NPs in PBS at a concentration at 20 mg/mL even in the presence of fetal bovine serum (FBS). As shown in Table S1, the HBPFPE-0 polymer has a high fluorine content (~13.8 wt

DOI: 10.1021/acsnano.8b03726
ACS Nano 2018, 12, 9162−9176

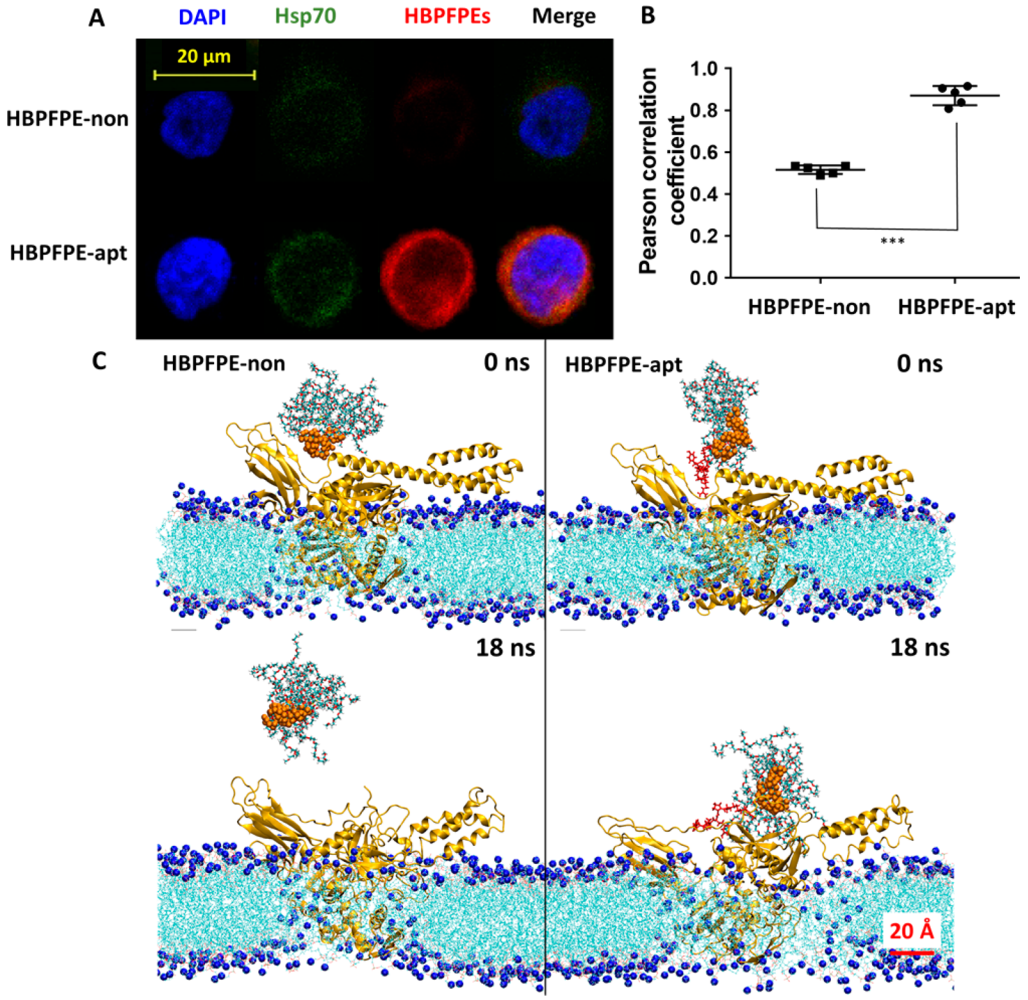

Figure 3. Comparison of cell uptake of aptamer-conjugated HBPFPE-apt and unconjugated HBPFPE-non. (A) Intracellular colocalization of HBPFPE nanoparticles and Hsp70 protein. MDA-MB-468 breast cancer cells grown on glass coverslips, were incubated with Cy5.5-labeled HBPFPE nanoparticles (red; 0.1 mM in culture medium) without the addition of free aptamer for 1 h, 37 °C, then fixed with 2% PFA, stained with Cy2-conjugated anti-Hsp70 antibody (green) and nuclei counterstained with DAPI (blue). Single color images were taken with a confocal microscope. (B) Quantitative analysis of the colocalization of HBPFPE nanoparticles and Hsp70 protein. Student's *t*-tests were performed with five single cells for each case (*$P < 0.001$). (C) Snapshots taken at 0 and 18 ns of the atomistic molecular dynamics simulation illustrating the contact between the HBPFPE nanoparticles and Hsp70 protein on the cell surface. The aptamer is red, the Hsp70 protein is shown in yellow, the PFPE segments are orange, and the cell membrane is shown in dark and light blue.**

%) and long ^{19}F NMR T_2 (86.5 ms), indicating likely high imaging intensity. The HBPFPE-non NP (conjugated with Cy5.5 dye only) shows little change in its ^{19}F NMR properties compared with the polymer without dye. The HBPFPE-apt NP (conjugated with both aptamer and dye) has a fluorine content at ∼10 wt % and long ^{19}F NMR T_2 relaxation time (86.4 ms), indicating again the likely high ^{19}F MRI sensitivity of HBPFPE-apt.

The hydrodynamic diameters (D_h) of HBPFPE-non and HBPFPE-apt, determined by ^{19}F diffusion-ordered spectroscopy (^{19}F DOSY) NMR, were below 10 nm indicating the absence of large aggregates despite the high fluorine content (Table S1). The absence of strong intermolecular interactions ensures high mobility of the fluorinated segments and hence sharp and intense ^{19}F NMR signals. Several previous reports have shown that a high fluorine content in polymers can lead to significant aggregation of the fluorinated segments and subsequent decreased segmental mobility.[23,37] It should be noted that the NMR experiments were performed in the presence of FBS, in order to simulate biological conditions. The use of ^{19}F DOSY NMR for the measurement of D_h offers significant advantages over dynamic light scattering (DLS) and ^{1}H DOSY NMR in complex media such as simulated biological environments or in the presence of fluorophores.[38,39]

In order to demonstrate the advantages of PFPE as the fluorinated moiety, and the importance of the incorporation of the OEGA block prior to formation of the HBP, we prepared two additional copolymers. HBPFPE-0' was prepared by RAFT copolymerization of OEGA and EGDMA directly using the PABTC−PFPE macro-CTA (Scheme S1), i.e., without the OEGA spacing block. Second, HBTFEA, a hyperbranched polymer incorporating 2,2,2-trifluoroacrylate was prepared using PABTC as the RAFT agent (Scheme S1, Table S1, Figures S8 and S9). Compared with HBPFPE-0, both control polymers exhibited a reduction in segmental motion as evidenced by shorter ^{19}F NMR T_2 relaxation times (49.3 and 30.7 ms for the HBPFPE-0′ and HBTFEA polymer, respectively). Such reduction in T_2 can lead to line broadening and attenuation of the ^{19}F NMR/MRI signal, and highlights the importance of maintaining high segmental mobility in ^{19}F

DOI: 10.1021/acsnano.8b03726
ACS Nano 2018, 12, 9162−9176

MRI agents.[5,19,27,40,41] The ^{19}F MRI performance of the HBPFPE nanoparticles was assessed by imaging of a range of solutions of varying concentration (Figure 2C). The excitation and refocusing pulses were centered on the largest peak in the ^{19}F NMR spectrum at around −82 ppm (Figure 2B). A linear dependence of signal-to-noise (SNR) can be observed for polymer concentrations in solution from 2.5 to 40 mg/mL. A small but measurable signal was observed for the lowest concentration of 2.5 mg/mL (~15 and 13 mM fluorine for the HBPFPE-non and HBPFPE-apt, respectively) (Figure 2D). This linear relationship between sample concentration and SNR indicates that the MRI signal intensity was dependent only on the fluorine concentration. Highly fluorinated materials have a tendency to aggregate in solutions at high concentrations, usually leading to a reduction in ^{19}F T_2 (thus broadened resonances) and reduced imaging intensities. To confirm this behavior, the ^{19}F NMR relaxation times T_1 and T_2 as well as D_h were measured at different solution concentrations, and are listed in the table in Figure 2E and Table S1. Both relaxation times and sizes did not change over this concentration range, indicating negligible change in spectral densities of high (T_1) or low (T_2) frequency motions and aggregation states. These results lead us to conclude that the HBPFPE nanoparticles are promising quantitative ^{19}F MRI contrast agents with high sensitivity.

Investigate the Binding Efficiency of the HBPFPE Nanoparticles to Hsp70 Protein. In order to investigate the binding efficiency of the HBPFPE nanoparticles to tumor cells, *in vitro* assays were conducted on MDA-MB-468 breast cancer cells, which are known to overexpress the Hsp70 protein.[42] Experiments were conducted using both HBPFPE-non without attached aptamer and HBPFPE-apt conjugated with both attached dye and aptamer. It was expected that HBPFPE-apt would show significant enhancement in cellular uptake as compared to HBPFPE-non, since it has been widely reported that the PEG-based polymers show negligible nonspecific binding with these cells over short incubation times.[43] To validate this hypothesis, cells were incubated for 2 h in the absence of polymer or in the presence of HBPFPE-non or HBPFPE-apt. As illustrated in Figure S10, flow cytometry showed that both the number of cells taking up polymer (84.2% vs 34.3%) and mean fluorescence intensity (9.7×10^6 vs 5.8×10^6) of the cells incubated with the aptamer-conjugated HBPFPE-apt are significant higher than for HBPFPE-non which lacks the targeting aptamer. Confocal microscopy images further confirmed significant uptake of the aptamer-conjugated polymer, with fluorescence detected through the Cy5.5 channel and shown in red color, but much reduced Cy5.5 fluorescence observed for cells incubated with HBPFPE-non (Figure S11). The combined flow cytometry and confocal results suggest that the HBPFPE nanoparticles with attached aptamer exhibit significantly higher uptake into the MDA-MB-468 cells, making them good candidates for detection of breast cancer tissue *in vivo* with high specificity.

The specific nature of the binding of the aptamer to Hsp70 was examined by immunofluorescence staining followed by confocal microscopy analysis. The presence of Hsp70-binding sites at the cell surface (green) was confirmed and shown in Figures 3A and S12. Enhanced red fluorescence of cells incubated with the HBPFPE-apt nanoparticle but without the free aptamer indicates the higher uptake of HBPFPE-apt compared with HBPFPE-non. Quantitative analysis of the image data revealed that the colocalization of HBPFPE nanoparticle with Hsp70 was significantly increased by conjugation to the aptamer (Figure 3B). Furthermore, incubation in the presence of free aptamer significantly reduced the uptake of HBPFPE-apt, but had no obvious effect on the uptake of HBPFPE-non (Figure S13). These results clearly demonstrate that conjugation to the aptamer allows the nanoparticle (HBPFPE-apt) to be recognized specifically by Hsp70 located on the surface of cells, and leads to an enhanced cellular uptake.

Atomistic molecular dynamic (MD) simulations were performed to help understand, at the molecular level, interactions between the HBPFPE nanoparticles (with or without attached aptamer) and Hsp70 protein on the surface of the cell membrane.[44] To reduce the computation time, MD simulations were conducted on a linear PFPE-based polymer (20 units of OEGA and one PFPE segment, poly$(OEGA)_{20}$-PFPE). The Hsp70 protein has two major functional domains: an N-terminal nucleotide-binding domain (NBD) of ~40 kDa and a C-terminal substrate-binding domain (SBD) of ~30 kDa, connected by a hydrophobic linker.[35,45] In the current simulation, the Hsp70 protein was inserted into the cell membrane with the SBD domain exposed. The interactions of the polymer chain with the cell membrane were simulated under near-physiological conditions (150 mM NaCl) for approximately 18 ns.

Figure 3C shows snapshots from the MD simulations of the interactions of the polymers with the cell membrane with inserted Hsp70 protein. In the case of HBPFPE-non, the polymer was not observed to interact with the Hsp70 protein for further insertion into the interior of the lipid bilayer. Therefore, the cellular uptake of HBPFPE-non was not a result of the specific binding and recognition with the Hsp70 protein. However, other uptake pathways, such as passive diffusion, could still be operative. (Figure 3C left). However, the incorporation of the aptamer in HBPFPE-apt changes dramatically the behavior. The aptamer was observed to specifically bind to the C-terminus of the SBD domain of the Hsp70 protein (Figure 3C right), leading to extended retention of HBPFPE-apt on the surface of cell membrane and thereby facilitating higher cellular uptake. The combination of MD simulations and experimental FACS and confocal studies of cellular uptake leads to a more complete understanding of how the highly fluorinated polymer interacts with the cell membrane in the presence of the Hsp70 protein.

Transport of the HBPFPE Nanoparticles across Cellular Barriers. To examine the transport of the HBPFPE nanoparticles across various barriers, auto- and pair correlation microscopy were employed. These methods allow the quantification of mobile HBPFPE nanoparticles, with and without the peptide aptamer functionalization, in subcellular compartments and the ease of transport across cell barriers such as the plasma membrane and the nuclear envelope.[46,47] The MDA-MB-468 cells were incubated with HBPFPE nanoparticles for 4 h, and then a continuous line scan measurement with a confocal microscope was performed spanning from the extracellular space (EXC) through the cytoplasm (CYTO) to the nucleus (NUC) of the cell under examination. The line scan then allowed acquisition of intensity kymographs for auto- and pair correlation analysis. The detailed workflow of the auto- and pair correlation analysis are shown in Figure S14.

DOI: 10.1021/acsnano.8b03726
ACS Nano 2018, 12, 9162−9176

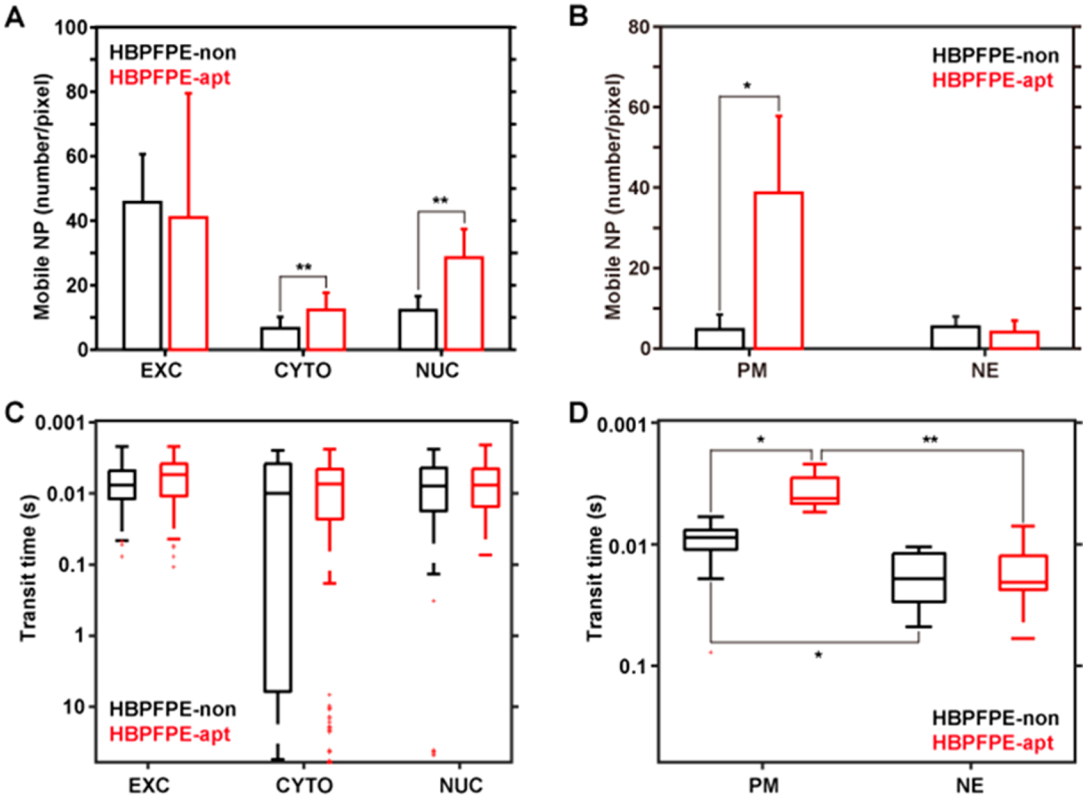

Figure 4. Measuring the subcellular distribution of HBPFPE nanoparticles and their mobility across subcellular barriers. Fluorescence intensity data were acquired along a line that spans from the extracellular space (EXC) to the cytoplasm (CYTO) and nucleus (NUC) of single cells. (A, B) Local concentration of mobile HBPFPE nanoparticles in the three cellular compartments and at the cellular barrier located pixels, the plasma membrane (PM) and nuclear envelope (NE), extracted from autocorrelation analysis. Error bars are standard deviation. (C, D) Transit times reflecting mobility within the cellular compartments and across the cellular barriers. For each condition five cells were analyzed and two line scans were acquired per cell. This resulted in $n = 10$ measurements; ns, not significant; $P > 0.05$; $^{*}P < 0.05$; $^{**}P < 0.01$ (t test).

The local distribution of mobile polymers in the three cellular compartments (EXC, CYTO and NUC) was calculated from the autocorrelation function, and shown in Figure 4A. It was observed that the concentration of mobile HBPFPE-apt in both the cytoplasm and nucleus was higher than HBPFPE-non. Significantly, the concentration of mobile HBPFPE-apt at the pixels (average of three pixels with a pixel size of 300 nm) corresponding to the location of the plasma membrane region was significantly higher than HBPFPE-non (38.7 and 4.7 particles per pixel, respectively, Figure 4B), while the modification with aptamer had no significant impact on the number of mobile HBPFPE nanoparticles at the nuclear envelope (average of three pixels). These observations indicate that the Hsp70 protein located on the cellular surface can aid the HBPFPE-apt polymers to cross the plasma membrane resulting in a higher particle concentration in the cytoplasm. Such a conclusion is in agreement with the immunofluorescence images in Figure 3. Additional studies of the mechanism of NPs crossing the plasma membrane, e.g. through passive diffusion or energy-dependent pinocytosis, will be reported separately as these measurements are complex and can be influenced by factors such as NP size, shape, and surface chemistry.[48]

The pair correlation function was applied to calculate the transit times of polymers within cellular compartments and crossing cellular barriers at a given distance ($\delta r = 8$ pixels, pixel size of 300 nm). This was performed by extracting the value of the transit time at the peak of the pair correlation function for every pixel along the imaged line. The transit times of HBPFPE-apt and HBPFPE-non exhibited no significant difference in the three subcellular compartments (Figure 4C). This similarity in transit times between the two polymers can be attributed to the similar size of HBPFPE-non and HBPFPE-apt. The transit times of the polymers crossing the two major cellular barriers (the plasma membrane and nuclear envelope) were also calculated and are shown in Figure 4D. These data indicate that passage of HBPFPE-apt across the plasma membrane was significantly faster than for HBPFPE-non; consistent with the observed higher cytoplasmic concentration of the aptamer-conjugated polymer. While it was found that the nuclear envelope constituted a more significant barrier for these polymers than the plasma membrane, no significant difference was observed in the number and transit times of the two types of polymer crossing the nuclear envelope. This is an important result as it suggests that the higher nuclear concentration of HBPFPE-apt in the nucleus was a result of the higher cytoplasmic concentration and not by an altered nuclear import/export mechanism. To be more specific, passive diffusion of HBPFPE-non and HBPFPE-apt across the nuclear envelope through the nuclear pore complexes (NPC) is believed to be the main pathway for the HBPFPE NPs entering into the nuclei. These NPs are small molecules ($M_w < 40$ kDa and $D_h < 10$ nm) and are able to pass through NPC by passive diffusion as shown in several previous studies.[49,50]

DOI: 10.1021/acsnano.8b03726
ACS Nano 2018, 12, 9162–9176

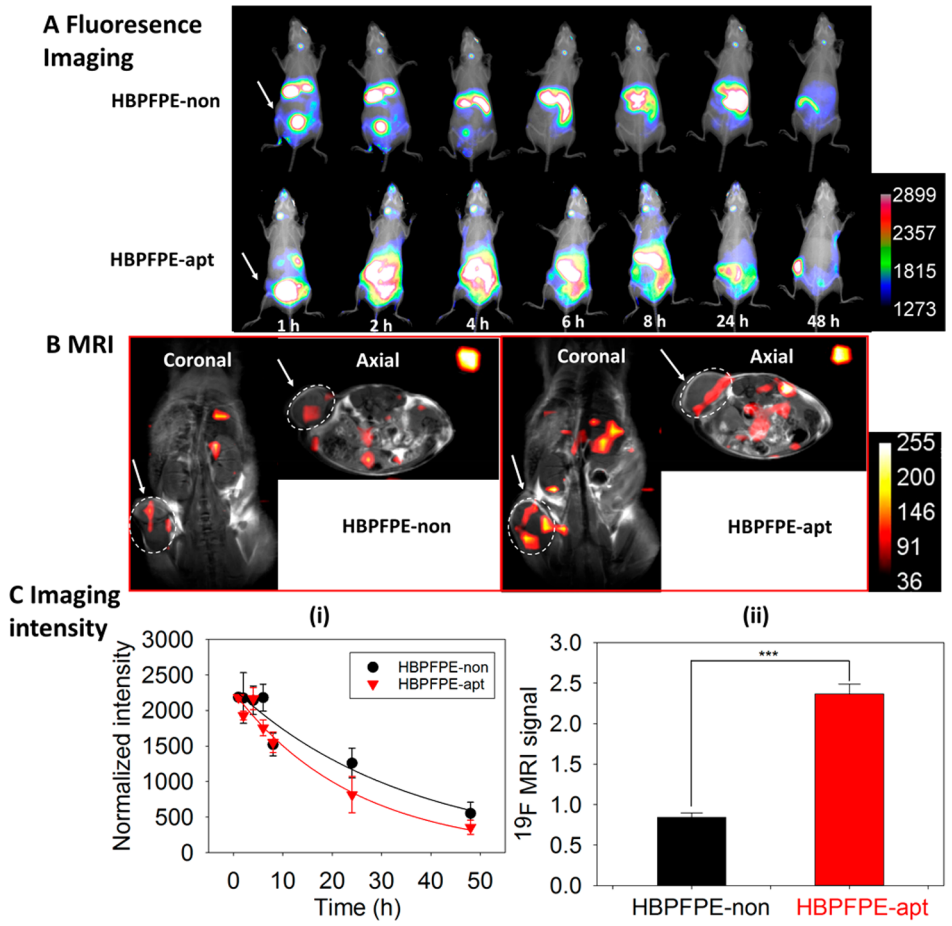

Figure 5. Demonstration of utility of HBPFPE nanoparticles for molecular imaging using a mouse subcutaneous MDA-MB-468 tumor model. For each mouse, 100 μL of HBPFPE-PBS solution (2 mmol fluorine per kg = 288 and 380 mg per kg or 5.8 and 7.6 mg/mouse for HBPFPE-non and HBPFPE-apt, respectively) were injected intravenously via the tail vein (n = 4/group). (a) Fluorescence images of mice following intravenous injection of HBPFPE-non and HBPFPE-apt at different time points from 1 to 48 h PI. Fluorescence images are coregistered with X-ray images of the mice following intravenous injection of the polymer solution. (b) Coronal and axial MRI images at 9.4 T of the tumor-bearing mice following intravenous injection of HBPFPE nanoparticles at 48 h PI. The high-resolution ^{1}H MR images are overlaid with the ^{19}F MR images (acquisition time: 1 min 36 s and 10 min 40 s for ^{1}H and ^{19}F MRI, respectively). A solution of HBPFPE-non in an NMR tube (300 μL of 5 mg/mL) was used as an internal reference. The white arrow in Figure 4A and B indicates the tumor sites. (C) Normalized fluorescence (i) and ^{19}F MRI (ii) intensities post injection of the HBPFPE nanoparticles. The half-lives of HBPFPE NPs were obtained by the first-order decay fitting of all data points in shown in Figure 5Ci. Data in (C) are mean ± standard deviation (SD). *** P < 0.001, Student's t test.

In summary, the correlation analysis revealed a higher concentration of mobile HBPFPE-apt compared to HBPFPE-non within the cytoplasm, and faster transport across the cytoplasm as well as a higher concentration in the nucleus. Thus, the data suggests a higher rate of uptake of aptamer-modified polymer into the cell, while the transport across the nuclear envelope, the rate-limiting step in nuclear accessibility, remained unaltered.

***In Vivo* Detection of Breast Cancer by ^{19}F MRI and Optical Imaging.** The effectiveness of the HBPFPE nanoparticles as dual-mode molecular imaging agents for specific detection of disease *in vivo* was demonstrated on a MDA-MB-468 subcutaneous murine tumor model (Figure 5). PBS solutions of either of the HBPFPE nanoparticles (ca. 2.0 mmol kg^{-1} ^{19}F) were administered to three mice (nine-week-old tumor-bearing female mice). It should be noted that the dose applied in the current study is much lower than previously reported for a partly fluorinated asymmetric molecule (ca. 30–60 mmol kg^{-1})[51] and PEI-LA-F$_3$ (ca. 7.5 mmol kg^{-1}),[26] indicating the outstanding *in vivo* ^{19}F MRI sensitivity of our HBPFPE nanoparticles.

As shown in Figure 5A and B, both ^{19}F MR and fluorescence images show clearly the presence of HBPFPE nanoparticles in the major organs after injection, highlighting the high intrinsic sensitivity and complementarity of these two imaging modalities. This dual-modal imaging agent combines the high sensitivity and relative low-cost advantages of fluorescence imaging with the capability of high anatomical resolution of MRI. As is illustrated in Figure 5A, the biodistribution of each HBPFPE polymer was determined at regular intervals, at 1, 2, 4, 6, 8, 24, and 48 h post injection (PI). In the initial 2 h post injection, the HBPFPE nanoparticles show similar excretion pathways through hepatic and renal clearance. It is widely reported that the clearance of molecules through renal excretion is highly size-dependent and neutral nanoparticles with <8 nm in diameter are able to pass through the renal fenestrations.[52] The sizes of the HBPFPE nanoparticles after the conjugation of dye and/or aptamer were measured by ^{19}F DOSY NMR in the presence of serum to be below 8 nm (6.5

DOI: 10.1021/acsnano.8b03726
ACS Nano 2018, 12, 9162–9176

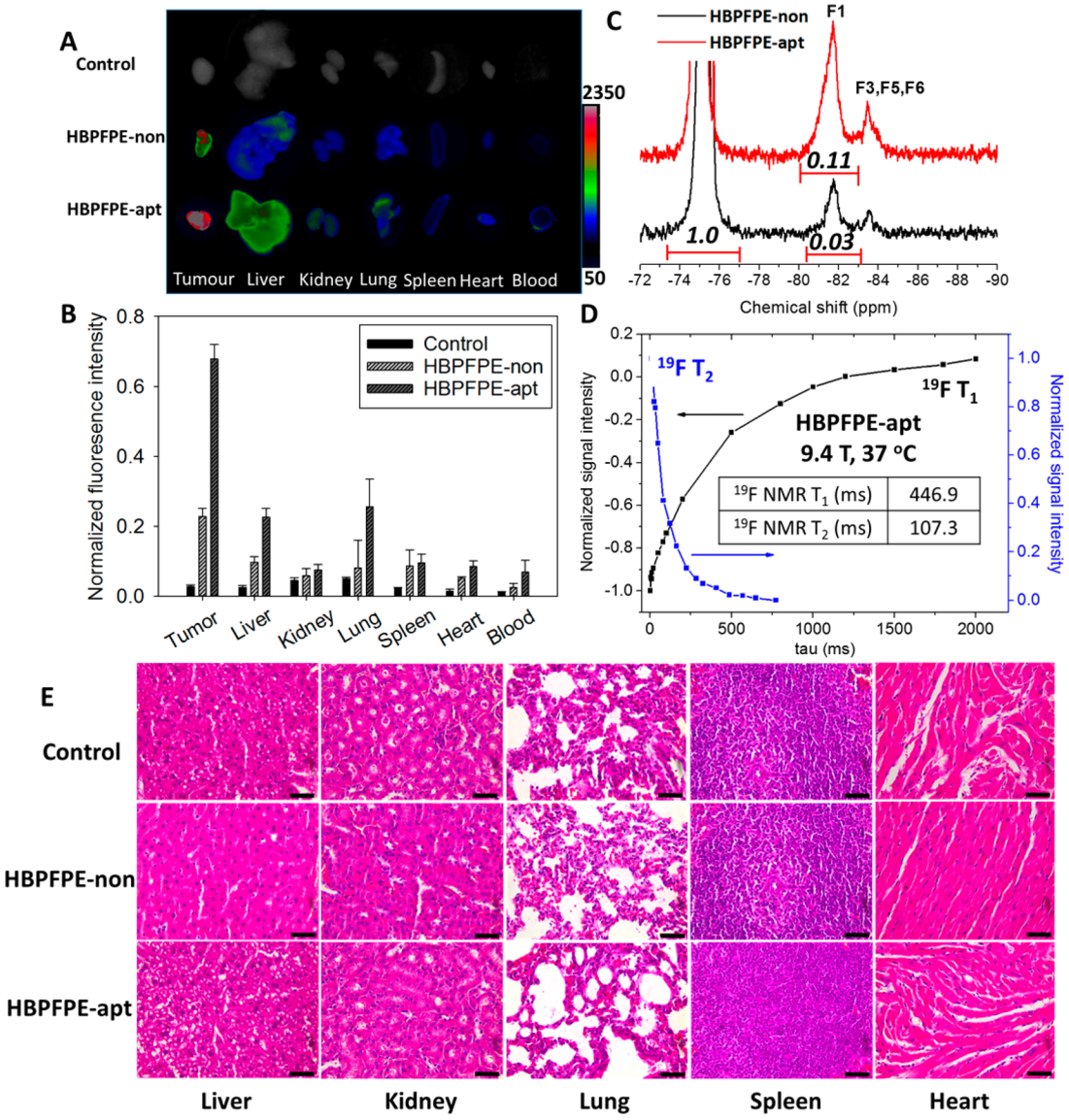

Figure 6. *Ex vivo* fluorescence, ^{19}F NMR, and histological analysis. (A) Coregistered X-ray and fluorescence images and (B) quantified biodistribution data collected *ex vivo* of harvested mice organs 48 h PI of PBS, HBPFPE-non and HBPFPE-apt. The plots are of the mean ± SD (n = 4 mice/group). (C) Intratumoral ^{19}F NMR spectra and (D) ^{19}F NMR T_1 and T_2 relaxation curves and times of polymer within the tumor 48 h after injection. The temperature was set to 37 °C during NMR acquisition. The relaxation times of the HBPFPE nanoparticles at a field strength of 9.4 T were measured for the peak F1. (E) Histological sections in the acute toxicity test (H&E staining, 40×). The scale bar represents 20 μm. There are no apparent histopathologic changes observed in the tissues, including lung, heart, liver, kidney, and spleen for both HBPFPE-non and HBPFPE-apt.

and 7.8 nm for HBPFPE-non and HBPFPE-apt, respectively; see Table S1 and Figure S15). Accumulation of polymer in the liver was also observed, indicating rapid recognition and uptake by the liver. This is in line with previous reports that the elimination of particles with a size range below 20 nm can occur through the normal drainage organs, such as the liver.[53,54] On the other hand, the incorporation of OEG segments in polymers has been widely reported to prolong the circulation time in blood and reduce the uptake by the mononuclear phagocyte system (MPS), such as the liver and lung.[55,56] It is likely that exposure of the hydrophobic PFPE segments of the HBPFPE polymer enhances recognition and filtration by the liver for hepatic clearance.

At longer times following injection, both HBPFPE nanoparticles were mainly detected in the liver and at 48 h post injection the fluorescence signals from the whole body (excluding the tumor region) were negligible, indicating that clearance of the HBPFPE nanoparticles from the body was complete after approximately 2 days. However, much stronger fluorescence can be observed in the tumor region after injection of HBPFPE-apt compared to HBPFPE-non. This highlights the efficiency of the aptamer as a targeting ligand for *in vivo* recognition of breast cancer cells, in line with the *in vitro* cell uptake results shown in Figures 3 and 4. In addition, at the study end point at 48 h PI, detailed *ex vivo* biodistribution studies were performed as discussed in a later section.

Quantitative fluorescence imaging has been widely applied to determine the biodistribution and half-lives of nanoparticles *in vivo*.[57,58] Therefore, in the current study normalized fluorescence intensities over the whole body region were measured using the Fiji software and plotted as a function of time to generate biodistribution profiles of the HBPFPE

DOI: 10.1021/acsnano.8b03726
ACS Nano 2018, 12, 9162–9176

nanoparticles (Figure 5Ci). On the basis of the decay in fluorescence intensity of the whole body the *in vivo* residence half-life, $t_{1/2}$, of the HBPFPE nanoparticles was estimated by the first-order fitting of the decay in fluorescence intensity to be approximately 26.1 and 17.6 h for HBPFPE-non and HBPFPE-apt, respectively. In comparison, the *in vivo* residence half-lives of perfluorocarbon nanoemulsions are reported to be months or longer.[24,51,59] The much faster clearance of the HBPFPE nanoparticles from the body highlights one of the main advantages of the HBPFPE nanoparticles as ^{19}F MRI CAs. ^{19}F MRI offers rich functional and pharmacokinetic information. Furthermore, the combination of ^{1}H and ^{19}F MRI can be achieved by superimposing the highly selective ^{19}F images over the high-resolution anatomical ^{1}H images through the use of doubly tuned MRI coils, which are becoming available in many hospitals. As shown in Figure 5B, ^{19}F MR images of mice along with a reference tube (^{19}F signal intensity set to be 1.0) were acquired to visualize and quantify the distribution of the HBPFPE nanoparticles in various tissues. Both coronal and axial MR images (the ^{1}H MR images are overlaid with the ^{19}F images) were acquired at 48 h post injection of the HBPFPE nanoparticles. *In vivo* ^{19}F MR signals of both HBPFPE nanoparticles can be clearly detected in the tumor region, indicating again the outstanding sensitivity of the HBPFPE nanoparticles as ^{19}F MRI contrast agents. The amount of HBPFPE polymer within the tumor volume was calculated by comparison with the signal intensity of the reference tube. At 48 h following injection of the HBPFPE nanoparticles, the intratumoral content of polymer was found to be 0.84 and 2.37 for HBPFPE-non and HBPFPE-apt, respectively (numbers are relative to the intensity of the reference tube). The enhanced accumulation (2.8 times larger) of the aptamer-conjugated HBPFPE-apt in the tumor is in line with the results of *in vitro* cellular uptake and *in vivo* fluorescence imaging studies, indicating again the high efficiency of the aptamer as a targeting ligand for detection of breast cancer. Notably, although most of the injected PFPE-based polymer was excreted after 48 h, the ^{19}F signal could be still detected in the liver (Figure 5B). This observation could be result of digestion of the HBPFPE in the liver; however, we have no direct evidence of degradation. Alternatively, the change in T_2 relaxation time could reflect that the local environment experienced by the molecule *in vivo* is different from that used in the *in vitro* experiments. We have previously shown that the conformational and NMR properties of partly fluorinated polymers of this and similar structure are very sensitive to the local environment, e.g., pH, ionic strength.[5,6,20] These observations therefore highlights the challenges of designing highly stable or discrete fluorinated imaging agents for ultrafast and uniform clearance from the liver.[60]

Several additional points need to be highlighted for the current study. First, the tumor model we used in this proof-of-concept study was a subcutaneous tumor model with diameter of ∼1 cm. Future studies will investigate the detection limits of PFPE-based polymers in orthotopic models with smaller tumor sizes (diameter <1 cm). Second, in the current ^{19}F MRI experiments, one slice was acquired to gain maximum signal intensity for elucidating NP accumulation in tumor. In future studies, multiple slice ^{19}F MR images with smaller slice thickness will be collected to improve the imaging resolution. Finally, the balance between the imaging efficiency and clearance rate should be taken into careful consideration. In this study, the HBPFPE-apt polymer provides high intratumoral ^{19}F MRI signal, and sufficient imaging SNR for the detection of breast cancer. Given such a high imaging sensitivity, fast clearance is preferred to reduce the potential for toxicity to normal organs. Overall, however, the *in vivo* ^{19}F MRI experiments conducted in this study provide an exciting example of the application of PFPE-based polymeric imaging agents for specific detection of diseases *in vivo* by ^{19}F MRI, and will accelerate the clinical translation of these HBPFPE polymers.

***Ex Vivo* Evaluation of Biodistribution and NMR Properties of the HBPFPE Nanoparticles.** At the study end point at 48 h PI, the tissue and organs were harvested (tumor, liver, kidney, lung, spleen, heart, and blood) and *ex vivo* fluorescence images measured to obtain information on the end point biodistribution (Figure 6A). The biodistribution was then determined by dividing the fluorescence intensity of each organ by the weight of the organ. As shown in Figure 6B, both HBPFPE nanoparticles remained largely in the tumors due to the enhanced permeability and retention (EPR) and/or specific ligand interaction effects. To be more specific, the intratumoral fluorescence intensity for HBPFPE-apt is approximately 3-fold higher than that for HBPFPE-non, revealing again the high efficiency in recognition and uptake by cancer cells of the aptamer-conjugated HBPFPE-apt. The relatively high fluorescence signal observed in the liver might be due to the phagocytosis of particles via the MPS, because signals from other organs involved in the MPS, such as the lung and kidney, can be also observed. This observation was supported by the conclusions obtained from the *in vivo* biodistribution study, which showed that the NPs can be taken up and cleared by the MPS, and that NPs with conjugated aptamer showed much higher signal intensity than the nonconjugated molecules. We did not observe penetration through the blood-brain barrier (BBB) for both HBPFPE polymers, due to the high molecular weight of the polymer (>20 kDa). It was previously reported that the BBB can restrict entry by NPs with molecular weight highers than ca. 600 Da.[61]

To understand further the behavior of the polymers *in vivo*, the ^{19}F NMR spectra and relaxation times of the HBPFPE nanoparticles within the excised tumor (48 h PI) were measured and are shown in Figure 6C and D. These important measurements provide information on whether fluorine mobility (and hence imaging performance) changes with pH or different redox environments that are typically encountered within the intracellular compartments.[21] A tube containing a solution of TFA was again used as the internal reference for both chemical shift and intensity (set to −76.55 ppm and 1.0, respectively) of peaks in the NMR spectrum of the PFPE segments. As shown in Figure 6C, the integrals of the fluorinated methyl and methylene chemical group in HBPFPE nanoparticles (peak F1, Figure 2B) were measured to be 0.03 and 0.11 (compared with the TFA reference) for tumor containing HBPFPE-non and HBPFPE-apt, respectively. These values are in strong agreement with the *in vivo* observations, where the fluorescence and ^{19}F MRI signal intensities of tumors are higher for HBPFPE-apt compared with HBPFPE-non. These experiments suggest that the specificity of the PFPE-based polymer for MDA-MB-468 tumors *in vivo* is significantly enhanced by conjugation with the aptamer.

The ^{19}F NMR T_1 and T_2 relaxation times of HBPFPE-apt were also measured to evaluate the mobility of the PFPE segments within the tumor cells at 37 °C (Figure 6D). The T_1

DOI: 10.1021/acsnano.8b03726
ACS Nano 2018, 12, 9162−9176

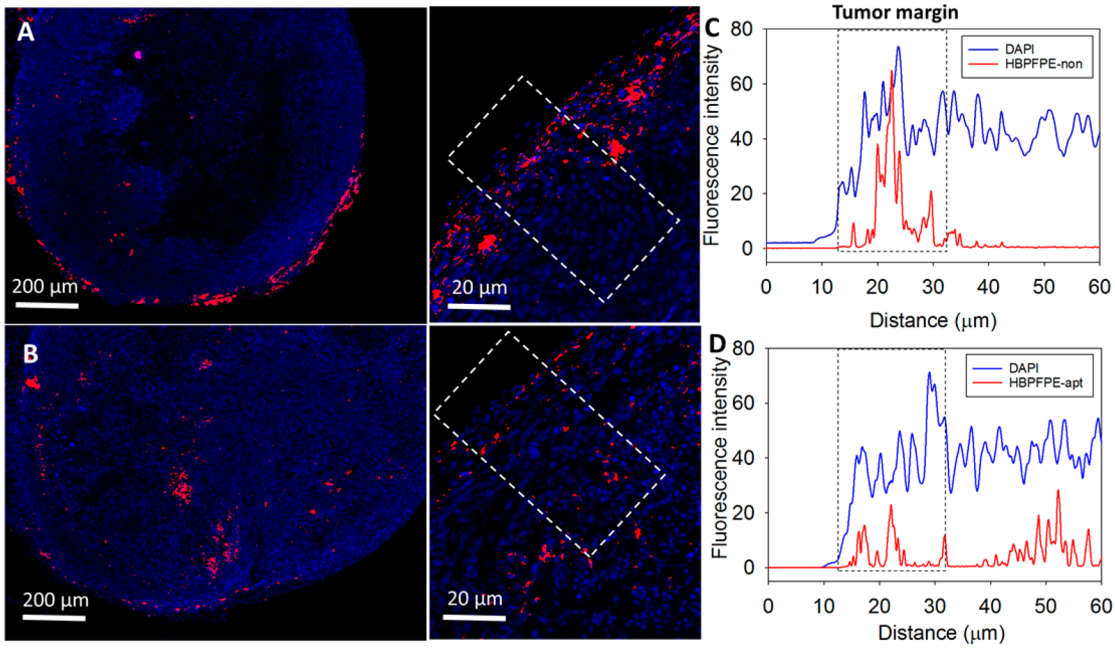

Figure 7. Intratumoral distribution and penetration of HBPFPE nanoparticles. Representative fluorescence micrographs of tumor sections 48 h PI of (A) HBPFPE-non and (B) HBPFPE-apt. The images were taken at low magnification with 2.5× (left) and high magnification with 20× (right) objectives, respectively. (C, D) Averaged DAPI and Cy5.5 fluorescence intensities in a selected rectangle regions drawn from outside to inside of the tumor section (blue = DAPI and red = HBPFPE nanoparticles).

and T_2 relaxation times were measured using the standard inversion−recovery and Carr−Purcell−Meiboom−Gill (CPMG) pulse sequences, respectively. Importantly, a high ^{19}F T_2 at 107.3 ms was obtained, indicating high intratumoral segmental mobility of the fluorinated segments. It can be thus concluded that the cellular internalization of the polymer does not appreciably affect the NMR and MRI properties. This measurement is an important example of testing the ^{19}F NMR performance of fluorinated polymers in real-tumor environments.

In order to assess the toxicity of the HBPFPE nanoparticles, we examined the effect of the administration of HBPFPE nanoparticles on normal organs, including liver, kidney, lung, spleen, and heart, by hematoxylin and eosin (H&E) stains. As shown in Figure 6E, no noticeable sign of organ damage was observed from the H&E stained organ slices, suggesting the safety of applying HBPFPE nanoparticles as molecular imaging agents. Furthermore, the *in vitro* cytotoxicity of the HBPFPE nanoparticles was tested against MDA-MB-468 breast cancer cells via an MTS cell viability assay. The HBPFPE nanoparticles had little effect on cell viability in the concentration ranges from 2 to 15 mg/mL at a 24 h incubation time (Figure S16).

The HBPFPE-Apt Nanoparticles Have Superior Tumor Penetration Performance. Having established that the aptamer-conjugated PFPE-based polymer has excellent binding efficiency to the MDA-MB-468 tumor, we proceeded to investigate the ability of these PFPE-based polymers to penetrate a solid tumor. For this purpose, MDA-MB-468 tumor-bearing mice were intravenously injected with HBPFPE nanoparticles and the tumors excised 48 h PI for paraffin embedding. Transverse tissue sections through the whole tumor (thickness = ∼8 μm) were examined by fluorescence microscopy. Fluorescence images of the tumor sections were obtained after applying mounting media containing DAPI for staining the nuclei. The distribution of the polymers is displayed in Figures 7 and S17. The Cy5.5 signal from HBPFPE-non was detected primarily in the periphery of the tumor while the aptamer-conjugated HBPFPE-apt can be found largely in the interior of the tumor (shown in red). The intratumoral distribution of the HBPFPE nanoparticles with or without attached aptamer was also analyzed by measuring the variation in the fluorescence intensity within a rectangular section drawn from inside of the tumor to a remote area (Figure 7C and D). Consistent with fluorescence microscopy observations, the Cy5.5 signal peaks of HBPFPE-non can be only observed when the line crosses the surface of the tumor. In sharp contrast, intense Cy5.5 signal can be detected in both the interior and periphery of the tumor, indicating greater penetration of the aptamer-conjugated HBPFPE-apt.[30] These outcomes indicate that the aptamer-conjugated PFPE-based polymers can more readily penetrate throughout the center of solid MDA-MB-468 tumors. Tumor penetration is highly dependent on the polymer concentration at the surface of the solid tumor. Therefore, the low penetration to the inner parts of the tumor by HBPFPE-non is likely due to low accumulation of the polymer at the tumor surface. Alternatively the higher penetration of HBPFPE-apt could be due to specific binding between HBPFPE-apt and Hsp70 protein. Hsp70 protein was reported to be widely present in the intercellular space.[62] Thus, binding to the Hsp70 protein can accelerate the transport of HBPFPE-apt from the surface to inner parts of the tumor through the intercellular spaces.[63] Meanwhile, previous reports have also revealed that conjugation of aptamer can not only enhance penetration of the tumor but also can increase the retention time in the tumor.[30,64] The higher capacity for tumor penetration of HBPFPE-apt is likely to be important for theranostic applications.

DOI: 10.1021/acsnano.8b03726
ACS Nano 2018, 12, 9162−9176

CONCLUSIONS

In summary, we have developed a PFPE-based platform for the preparation of multifunctional polymeric ^{19}F MRI CAs for *in vivo* detection of breast cancer cells by both fluorescence imaging and ^{19}F MRI. These HBPFPE nanoparticles have the highest fluorine content and imaging sensitivity reported for polymeric ^{19}F MRI CAs. The structural characteristics, ^{19}F NMR and MRI properties, *in vitro* cell uptake, intracellular distribution and trafficking, *in vivo* and *ex vivo* molecular imaging, as well as tumor-penetration are studied in detail. The results collectively indicate that the PFPE-based ^{19}F MRI CAs conjugated with targeting aptamers are excellent candidates for the specific detection of breast cancer *in vivo* by ^{19}F MRI. The much faster clearance of these PFPE-based polymers nanoparticles compared with perfluorocarbon-based emulsions ($t_{1/2}$, ~ 20 h vs months) is expected to significantly reduce the burden to normal organs. Moreover, the extensive tumor-penetration of the aptamer-conjugated nanoparticles highlights that these imaging agents can be applied for both effective diagnosis and treatment of diseases. Our study indicates that the PFPE-based nanoparticles are promising ^{19}F MRI CAs for detection of diseases *in vivo*, and provides critical design parameters for fluorinated polymeric imaging agents.

EXPERIMENTAL SECTION

Materials. All chemicals were purchased from Sigma-Aldrich unless otherwise stated. Oligo(ethylene glycol) methyl ether acrylate (OEGA, M_W = 480 g/mol), ethylene glycol dimethyl acrylate (EGDMA), and 2,2,2-trifluoroethyl acrylate (TFEA) were passed through basic alumina columns to remove inhibitors prior to use. Monohydroxy perfluoropolyether (PFPE-OH, ~1450 g/mol) was supplied by Apollo Scientific Ltd., UK. 2,2′-Azobis(2-methylpropionitrile) (AIBN) was recrystallized twice from methanol before use. The RAFT agent (propanoic acid)yl butyl trithiocarbonate (PABTC) were synthesized according to a previously reported procedure.[65] Cyanine5.5 maleimide was purchased from Lumiprobe. Milli-Q water with a resistivity of 18.4 MΩ/cm was used for the relevant experiments. The dialysis tubing with molecular weight cutoff (MWCO) of 3.5 kDa was purchased from Thermo Fisher Scientific Inc. and Spectrum Laboratories Inc., respectively.

Dulbecco's modified Eagle's medium (DMEM) with high glucose, phosphate-buffered saline (PBS), Tryple Express, fetal bovine serum (FBS) and antibiotic-antimycotic (AA) were purchased from ThermoFisher Scientific. Mounting media with DAPI was purchased from Vector Laboratories. CellTiter 96 AQ_{ueous} One solution cell proliferation assay (MTS) was purchased from Promega. The MDA-MB-468 cell line (ATCC HTB-132) was purchased from American Type Culture Collection (ATCC). Anti-Hsp70 antibody (2A4; ab5442) was obtained from Abcam (Cambridge, UK), and anti-mouse IgM secondary antibody and streptavidin Cy2 were from Jackson ImmunoResearch (West Grove, PA).

The peptide aptamer with maleimide modification was synthesized by Mimotopes Australia with peptide sequence as follows: SPWPRPTY (M_w = 1196.2 Da). The mass and ^{1}H NMR spectra are shown in Figure S4.

NMR Spectroscopy. ^{1}H NMR spectra were obtained of solutions of the polymer in $CDCl_3$ using a Bruker Avance 400 MHz (9.4 T) spectrometer to analyze the conversion of monomer to polymer and the structure of the polymers. Solution spectra were measured under the following measurements conditions: 90° pulse width 14 μs, relaxation delay 1 s, acquisition time 4.1, and 32 scans. Chemical shifts are reported relative to the residual solvent peak.

^{19}F NMR spectra were acquired using a Bruker Avance 400 MHz spectrometer with PBS/D_2O (90/10, v/v) as solvent with the presence of 10% fetal bovine serum (FBS). The ^{19}F NMR spectra of tumors were collected by squeezing the tumor in a 5 mm NMR tube filled with PBS/D_2O solution. The spectra were measured under the following measurements conditions: 90° pulse width 15 μs, relaxation delay 2 s, acquisition time 0.73 and 64 scans.

^{19}F spin−spin relaxation times (T_2) were measured using the Carr−Purcell−Meiboom−Gill (CPMG) pulse sequence at 310 K. The samples were dissolved in PBS/D_2O (90/10, v/v) in the presence of FBS at a concentration of 20 mg/mL. The 90° pulse was determined by dividing with a 360° pulse width, at which the NMR signal is zero. The relaxation delay was 2 s and the number of scans is 16. The relaxation times for the major peaks only are reported.

^{19}F spin−lattice (T_1) relaxation times were measured using the standard inversion−recovery pulse sequence. For each measurement, the relaxation delay was 2 s and the number of scans was 16. Only values for the major peaks are reported.

The ^{19}F NMR T_1 and T_2 relaxation times of the tumor were collected under similar conditions as described above. The number of scans were increased to 256 due to the lower ^{19}F signal in tumor than that in solution.

^{19}F NMR diffusion-ordered spectroscopy (DOSY) was conducted for determination of size of polymer in serum. Diffusion coefficients (D) for each sample were calculated by fitting the decay of NMR signal intensity to a monoexponential function. The D_h was then calculated by applying the Einstein−Stokes equation:

$$D_h = k_B T/(3\pi\eta D)$$

where η is the dynamic viscosity, T is the absolute temperature, and k_B is the Boltzmann constant.

Fluorescence Microscopy. For the experiments presented in Figures 1A, S11, S12 and S13: cells were seeded into a 24-well plate on coverslips and incubated with polymer solutions (100 μM in complete medium). Following 2 h incubation, the cells were washed twice with PBS, then cells were fixed in 4% paraformaldehyde (PFA) solution (0.5 mL) for 10 min at 37 °C. The PFA was then removed and the cells washed twice with PBS and once with water. Nuclei were stained by incubation of fixed cells with DAPI for 10 min. Coverslips were then mounted onto glass microscope slides for examination under a confocal microscope Zeiss LSM 710.

For the experiments presented in Figure 4, Cy5.5-labeled HBPFPE-non and HBPFPE-apt polymers were measured using 633 nm excitation and 656−758 nm emission ranges. Then a line scan was performed going from the extracellular matrix into the nucleus.

Auto- and Pair Correlation Data Analysis. The auto- and pair correlation analysis was conducted as described previously[37] using a custom written Matlab code (available on request). In brief, the autocorrelation function ($G(\tau)$) is calculated using the following expression:

$$G(\tau) = \frac{\langle F(t)\, F(t+\tau)\rangle}{\langle F(t)^2\rangle} - 1$$

Where $F(t)$ is the fluorescence intensity at time t and $F(t + \tau)$ is the fluorescence intensity after a delay time, τ. We use the amplitude of $G(\tau)$ at $\tau = 0$ ($G(0)$) to extract the number of molecules (N) in each pixel along the line scan using the following function, where γ describes the excitation volume shape (γ = 0.3536 for a one photon point spread function three-dimensional Gaussian distribution):

$$N = \frac{\gamma}{G(0)}$$

To obtain the pair correlation function (pCF), fluorescence fluctuations between two points at a distance δr as a function of the transit time τ is calculated using the following expression:

$$G(\tau, \delta r) = \frac{\langle F(t, 0)\, F(t+\tau, \delta r)\rangle}{\langle F(t, 0)\, F(t, \delta r)\rangle}$$

The maximum peak of the derived pCF profile gives the average time a molecule takes to travel the given distance (δr was set to 8 pixels in this case with pixel size of 300 nm). A threshold was applied to reject low-amplitude correlation due to background for single-channel experiments (threshold = 0.1 of the maximum peak).

DOI: 10.1021/acsnano.8b03726
ACS Nano 2018, 12, 9162−9176

Immunofluorescence Staining. MDA-MB-468 cells were grown on glass coverslips at 37 °C in the presence or absence of free aptamer, then washed with PBS and fixed in 2% PFA. Cells were blocked with 1% PBS-BSA for 15 min at room temperature. Cells were then incubated with anti-Hsp70 antibody (1:50, v/v) at room temperature for 2 h. After washing with PBS three times, the cells were incubated with anti-mouse IgM secondary antibody (1:200, v/v) for 1 h followed by streptavidin Cy2 (1:300, v/v) for another 1 h at room temperature. The cells were washed again and mounted on glass slides with DAPI. Finally, immunostained cells were analyzed using a confocal microscope (Zeiss LSM 710).

***In Vivo* Imaging Analysis.** Mouse experiments were performed using female Balb/c nu/nu mice that were bred at the University of Queensland animal house. The mice were 5 weeks old for all experiments. And all mice were housed in the animal facility of the Centre for Advanced Imaging, with free access to water and food. Ethical clearance was obtained from the University of Queensland for live mice testing (AIBN/338/16). The respiration rate of the mouse was monitored at all times during the imaging experiment. The mouse was anaesthetized with an i.p. injection of 65 mg/kg ketamine, 13 mg/kg xylazine, and 1.5 mg/kg acepromazine.

Prior to imaging experiments, each mouse was injected subcutaneously with 3×10^6 MDA-MB-468 cells to the left flank. The fluorescence and MRI imaging experiments were performed about 30 days after tumor cell injections. For each mouse, 100 μL of polymer solution (2 mmol kg^{-1} of fluorine = 288 and 380 mg kg^{-1} body weight or 5.8 and 7.6 mg/mouse for HBPFPE-non and HBPFPE-apt, respectively) was injected through the tail vein to the tumor-bearing mouse once the tumor reached 1−1.2 cm in diameter.

Fluorescence and X-ray images were acquired using an *in vivo* MS FX Pro imaging station (Carestream Health, Inc., Woodbridge CT) at different time points post injection. Images were acquired via a pre-established three-step imaging protocol acquiring sequential fluorescence, reflectance and X-ray images. X-rays were collected with a standard 0.4 mm aluminum X-ray filter and an exposure time of 20 s using an X-ray energy of 35 KVP. Fluorescence images were collected at ex 630 nm and em 700 nm with a 20 s exposure. All Images were evaluated using Fiji imaging software. The half-lives of HBPFPE NPs were obtained by fitting the data points to a first-order decay function following a literature protocol.[55]

MRI images of live mice were taken on a Bruker BioSpec 94/30 USR 9.4 T small animal MRI scanner. Proton images were acquired using a rapid acquisition with relaxation enhancement (RARE) sequence (rare factor = 16, TE = 15.4 ms, TR = 1500 ms, FOV = 60 × 60 mm, matrix = 256 × 256, measurement time= 1 min 36 s and 8 × 5 mm slices). The ^{19}F images were acquired using RARE sequence (TE = 10 ms, TR = 1000 ms, number of averages = 80, FOV = 60 × 60 mm, matrix = 32 × 32, measurement time = 10 min 40 s, 1 × 30 mm slice). HBPFPE-non polymer solution in a NMR tube (300 μL of 5 mg/mL) was applied as internal reference. All the *in vivo* imaging experiments were repeated four times. Following the final time point, the animal was culled and organs were collected for *ex vivo* imaging and NMR measurements.

***Ex Vivo* Biodistribution Analysis.** Following the final time point, the mice treated with polymer were euthanized and the organs excised for *ex vivo* imaging using a Carestream MS FX Pro imaging station (Carestream Health, Inc., Woodbridge CT). The weight of organs and the volume of blood were recorded for normalization of the fluorescent intensity.

***Ex Vivo* Tissue Collection for Fluorescence Imaging.** *Ex vivo* tissue fluorescence imaging studies were performed using paraffin wax slices, four mice from each group were sacrificed at 48 h PI. The tumors were perfused with saline followed with 4% paraformaldehyde. Then the tissues were sampled for paraffin-embedding and preparation of tissue slices. After treatment with ethanol and xylene, tissues were covered with wax and place into a 60 °C vacuum oven for 45 min for slices preparation. Each organ was separated into ten pieces at two different positions (center and margin of tumor), each of which was cut into ∼8 μm thick sections. Lastly, sections were washed with PBS (3 × 5 min) and mounted with ProLong Gold antifade reagent. Sections were coverslipped and kept overnight at approximately 4−8 °C for curing prior to imaging. Slices of tissues were directly stained with 0.5 μg/mL of DAPI for 3 min. Images were captured with an Axioskop 40 microscope (Carl Zeiss, Göttingen, Germany) using an Axiocam MRm camera (Carl Zeiss). All images were acquired using a fixed exposure time (2.5× or 20×).

***Ex Vivo* Tissue Collection for NMR Analysis.** *Ex vivo* tumor NMR analyses were performed directly after the sacrifices of mice. In order to be fitted into a 5 mm NMR tube, tumors were smashed and suspended in 500 μL of PBS/D_2O (90/10, v/v). The acquisition temperature was set to be 37 °C.

Histopathologic Examination. After the mice were sacrificed, the lung, heart, liver, kidney, and spleen were quickly removed and immediately fixed in 4% paraformaldehyde, dehydrated in a graded series of alcohol, and then embedded in paraffin. Tissue sections (5 μm) were prepared and stained with hematoxylin and eosin. Thereafter, the sections were examined and microphotographed using a Leica DFC295 and DM 1000 Microsystem.

Statistical Analysis. *In vivo* and *ex vivo* experiments were repeated at least four times. The results are presented as the means ± SD. For the auto- and pair correlation microscopy, five cells were randomly selected and analyzed. Two line scans with different directions were acquired per cell. This resulted in $n = 10$ measurements for statistical analysis. The statistical analysis was done using Student's t test analysis. A p-value less than 0.05 was considered statistically significant. Significant value p ($^*p < 0.05$, $^{**}p < 0.01$, $^{***}p < 0.001$, and $^{****}p < 0.0001$).

ASSOCIATED CONTENT

Supporting Information

The Supporting Information is available free of charge on the ACS Publications website at DOI: 10.1021/acsnano.8b03726.

Additional experimental and characterization details, NMR spectroscopy, structure characteristics and of the HBTFEA and HBPFPE nanoparticles, and cell viability tests (PDF)

AUTHOR INFORMATION

Corresponding Author

*E-mail: a.whittaker@uq.edu.au.

ORCID

Cheng Zhang: 0000-0002-2722-7497
Hang Thu Ta: 0000-0003-1188-0472
Petr Král: 0000-0003-2992-9027
John Justin Gooding: 0000-0002-5398-0597
Andrew Keith Whittaker: 0000-0002-1948-8355

Notes

The authors declare no competing financial interest.

ACKNOWLEDGMENTS

The authors acknowledge the Australian Research Council (CE140100036, DP0987407, DP110104299, LE0775684, LE0668517, LE0882357, LE140100087, and LE160100168) and the National Health and Medical Research Council (APP1021759) for funding of this research. The Australian National Fabrication Facility, Queensland Node, is also acknowledged for access to some items of equipment. H.P. thanks the University of Queensland for her UQ Postdoctoral Research Fellowship for Women. C.Z. acknowledges the University of Queensland for his Early Career Researcher Grant (UQECR1720289). P.K. acknowledges the NSF Division of Materials Research Grant 1506886. We acknowledge Dr. Nyoman Kurniawan for assistance with the MRI measurements.

DOI: 10.1021/acsnano.8b03726
ACS Nano 2018, 12, 9162−9176

REFERENCES

(1) Chen, H.; Song, M.; Tang, J.; Hu, G.; Xu, S.; Guo, Z.; Li, N.; Cui, J.; Zhang, X.; Chen, X.; Wang, L. Ultrahigh 19F Loaded Cu1.75S Nanoprobes for Simultaneous 19F Magnetic Resonance Imaging and Photothermal Therapy. *ACS Nano* **2016**, *10*, 1355−1362.

(2) Nakamura, T.; Matsushita, H.; Sugihara, F.; Yoshioka, Y.; Mizukami, S.; Kikuchi, K. Activatable 19F MRI Nanoparticle Probes for the Detection of Reducing Environments. *Angew. Chem., Int. Ed.* **2015**, *54*, 1007−1010.

(3) Tirotta, I.; Dichiarante, V.; Pigliacelli, C.; Cavallo, G.; Terraneo, G.; Bombelli, F. B.; Metrangolo, P.; Resnati, G. (19)F Magnetic Resonance Imaging (MRI): from Design of Materials to Clinical Applications. *Chem. Rev.* **2015**, *115*, 1106−1129.

(4) Yu, J.-X.; Hallac, R. R.; Chiguru, S.; Mason, R. P. New Frontiers and Developing Applications in 19F NMR. *Prog. Nucl. Magn. Reson. Spectrosc.* **2013**, *70*, 25−49.

(5) Zhang, C.; Moonshi, S. S.; Peng, H.; Puttick, S.; Reid, J.; Bernardi, S.; Searles, D. J.; Whittaker, A. K. Ion-Responsive 19F MRI Contrast Agents for the Detection of Cancer Cells. *ACS Sensors* **2016**, *1*, 757−765.

(6) Zhao, W.; Ta, H. T.; Zhang, C.; Whittaker, A. K. Polymerization-Induced Self-Assembly (PISA) - Control over the Morphology of 19F-Containing Polymeric Nano-Objects for Cell Uptake and Tracking. *Biomacromolecules* **2017**, *18*, 1145−1156.

(7) Önal, E.; Zhang, C.; Davarcı, D.; İşçi, Ü.; Pilet, G.; Whittaker, A. K.; Dumoulin, F. Cyclotriphosphazene, A Scaffold for 19F MRI Contrast Agents. *Tetrahedron Lett.* **2018**, *59*, 521−523.

(8) Liu, Y.; Zhang, C.; Liu, H.; Li, Y.; Xu, Z.; Li, L.; Whittaker, A. Controllable Synthesis of Up-Conversion Nanoparticles UCNPs@ MIL-PEG for pH-Responsive Drug Delivery and Potential Up-Conversion Luminescence/Magnetic Resonance Dual-Mode Imaging. *J. Alloys Compd.* **2018**, *749*, 939−947.

(9) Xu, C.; Zhang, C.; Wang, Y.; Li, L.; Li, L.; Whittaker, A. Controllable Synthesis of A Novel Magnetic Core−Shell Nanoparticle for Dual-Modal Imaging and pH-Responsive Drug Delivery. *Nanotechnology* **2017**, *28*, 495101−495112.

(10) Kislukhin, A. A.; Xu, H.; Adams, S. R.; Narsinh, K. H.; Tsien, R. Y.; Ahrens, E. T. Paramagnetic Fluorinated Nanoemulsions for Sensitive Cellular Fluorine-19 Magnetic Resonance Imaging. *Nat. Mater.* **2016**, *15*, 662−668.

(11) Srinivas, M.; Turner, M. S.; Janjic, J. M.; Morel, P. A.; Laidlaw, D. H.; Ahrens, E. T. In *Vivo* Cytometry of Antigen-Specific T Cells Using 19F MRI. *Magn. Reson. Med.* **2009**, *62*, 747−753.

(12) Tirotta, I.; Mastropietro, A.; Cordiglieri, C.; Gazzera, L.; Baggi, F.; Baselli, G.; Bruzzone, M. G.; Zucca, I.; Cavallo, G.; Terraneo, G.; Baldelli Bombelli, F.; Metrangolo, P.; Resnati, G. A Superfluorinated Molecular Probe for Highly Sensitive *In Vivo* 19F-MRI. *J. Am. Chem. Soc.* **2014**, *136*, 8524−8527.

(13) Ashur, I.; Allouche-Arnon, H.; Bar-Shir, A. Calcium Fluoride Nanocrystals: Tracers for *In Vivo* 19F Magnetic Resonance Imaging. *Angew. Chem., Int. Ed.* **2018**, *57*, 7478−7482.

(14) Michelena, O.; Padro, D.; Carrillo-Carrion, C.; del Pino, P.; Blanco, J.; Arnaiz, B.; Parak, W. J.; Carril, M. Novel Fluorinated Ligands for Gold Nanoparticle Labelling with Applications in 19F-MRI. *Chem. Commun.* **2017**, *53*, 2447−2450.

(15) Boccalon, M.; Franchi, P.; Lucarini, M.; Delgado, J. J.; Sousa, F.; Stellacci, F.; Zucca, I.; Scotti, A.; Spreafico, R.; Pengo, P.; Pasquato, L. Gold Nanoparticles Protected by Fluorinated Ligands for 19F MRI. *Chem. Commun.* **2013**, *49*, 8794−8796.

(16) Fu, C.; Zhang, C.; Peng, H.; Han, F.; Baker, C.; Wu, Y.; Ta, H.; Whittaker, A. K. Enhanced Performance of Polymeric 19F MRI Contrast Agents through Incorporation of Highly Water-Soluble Monomer MSEA. *Macromolecules* **2018**, *51*, 5875−5882.

(17) Zhang, C.; Kim, D. S.; Lawrence, J.; Hawker, C. J.; Whittaker, A. K. Elucidating the Impact of Molecular Structure on the 19F NMR Dynamics and MRI Performance of Fluorinated Oligomers. *ACS Macro Lett.* **2018**, 921−926.

(18) Wang, K.; Peng, H.; Thurecht, K. J.; Puttick, S.; Whittaker, A. K. Segmented Highly Branched Copolymers: Rationally Designed Macromolecules for Improved and Tunable 19F MRI. *Biomacromolecules* **2015**, *16*, 2827−2839.

(19) Peng, H.; Thurecht, K. J.; Blakey, I.; Taran, E.; Whittaker, A. K. Effect of Solvent Quality on the Solution Properties of Assemblies of Partially Fluorinated Amphiphilic Diblock Copolymers. *Macromolecules* **2012**, *45*, 8681−8690.

(20) Thurecht, K. J.; Blakey, I.; Peng, H.; Squires, O.; Hsu, S.; Alexander, C.; Whittaker, A. K. Functional Hyperbranched Polymers: Toward Targeted *In Vivo* 19F Magnetic Resonance Imaging Using Designed Macromolecules. *J. Am. Chem. Soc.* **2010**, *132*, 5336−5337.

(21) Rolfe, B. E.; Blakey, I.; Squires, O.; Peng, H.; Boase, N. R. B.; Alexander, C.; Parsons, P. G.; Boyle, G. M.; Whittaker, A. K.; Thurecht, K. J. Multimodal Polymer Nanoparticles with Combined 19F Magnetic Resonance and Optical Detection for Tunable, Targeted, Multimodal Imaging *In Vivo*. *J. Am. Chem. Soc.* **2014**, *136*, 2413−2419.

(22) Fu, C.; Herbst, S.; Zhang, C.; Whittaker, A. K. Polymeric 19F MRI Agents Responsive to Reactive Oxygen Species. *Polym. Chem.* **2017**, *8*, 4585−4595.

(23) Du, W.; Nyström, A. M.; Zhang, L.; Powell, K. T.; Li, Y.; Cheng, C.; Wickline, S. A.; Wooley, K. L. Amphiphilic Hyperbranched Fluoropolymers as Nanoscopic 19F Magnetic Resonance Imaging Agent Assemblies. *Biomacromolecules* **2008**, *9*, 2826−2833.

(24) Yu, Y. B. Fluorinated Dendrimers as Imaging Agents for 19F MRI. *Wiley Interdiscip. Rev. Nanomed. Nanobiotechnol.* **2013**, *5*, 646−661.

(25) Kirberger, S. E.; Maltseva, S. D.; Manulik, J. C.; Einstein, S. A.; Weegman, B. P.; Garwood, M.; Pomerantz, W. C. K. Synthesis of Intrinsically Disordered Fluorinated Peptides for Modular Design of High-Signal 19F MRI Agents. *Angew. Chem., Int. Ed.* **2017**, *56*, 6440−6444.

(26) Guo, Z.; Gao, M.; Song, M.; Li, Y.; Zhang, D.; Xu, D.; You, L.; Wang, L.; Zhuang, R.; Su, X.; et al. Superfluorinated PEI Derivative Coupled with 99mTc for ASGPR Targeted 19F MRI/SPECT/PA Tri-Modality Imaging. *Adv. Mater.* **2016**, *28*, 5898−5906.

(27) Zhang, C.; Moonshi, S. S.; Han, Y.; Puttick, S.; Peng, H.; Magoling, B. J. A.; Reid, J. C.; Bernardi, S.; Searles, D. J.; Král, P.; Whittaker, A. K. PFPE-Based Polymeric 19F MRI Agents: A New Class of Contrast Agents with Outstanding Sensitivity. *Macromolecules* **2017**, *50*, 5953−5963.

(28) Moonshi, S. S.; Zhang, C.; Peng, H.; Puttick, S.; Rose, S.; Fisk, N. M.; Bhakoo, K.; Stringer, B. W.; Qiao, G. G.; Gurr, P. A.; Whittaker, A. K. A Unique (19)F MRI Agent for the Tracking of Non Phagocytic Cells *In Vivo*. *Nanoscale* **2018**, *10*, 8226−8239.

(29) Davydova, A. S.; Vorobjeva, M. A.; Venyaminova, A. G. Escort Aptamers: New Tools for the Targeted Delivery of Therapeutics into Cells. *Acta Nat.* **2011**, *3*, 12−29.

(30) Xiang, D.; Zheng, C.; Zhou, S.-F.; Qiao, S.; Tran, P. H.-L.; Pu, C.; Li, Y.; Kong, L.; Kouzani, A. Z.; Lin, J.; Liu, K.; Li, L.; Shigdar, S.; Duan, W. Superior Performance of Aptamer in Tumor Penetration over Antibody: Implication of Aptamer-Based Theranostics in Solid Tumors. *Theranostics* **2015**, *5*, 1083−1097.

(31) Brody, E. N.; Gold, L. Aptamers as Therapeutic and Diagnostic Agents. *Rev. Mol. Biotechnol.* **2000**, *74*, 5−13.

(32) Jayasena, S. D. Aptamers: An Emerging Class of Molecules That Rival Antibodies in Diagnostics. *Clin. Chem.* **1999**, *45*, 1628−1650.

(33) Jagadish, N.; Agarwal, S.; Gupta, N.; Fatima, R.; Devi, S.; Kumar, V.; Suri, V.; Kumar, R.; Suri, V.; Sadasukhi, T. C.; Gupta, A.; Ansari, A. S.; Lohiya, N. K.; Suri, A. Heat Shock Protein 70−2 (HSP70−2) Overexpression in Breast Cancer. *J. Exp. Clin. Cancer Res.* **2016**, *35*, 150−164.

(34) Calderwood, S. K.; Gong, J. Molecular Chaperones in Mammary Cancer Growth and Breast Tumor Therapy. *J. Cell. Biochem.* **2012**, *113*, 1096−1103.

(35) Rérole, A.-L.; Gobbo, J.; De Thonel, A.; Schmitt, E.; Pais de Barros, J. P.; Hammann, A.; Lanneau, D.; Fourmaux, E.; Deminov, O.; Micheau, O.; Lagrost, L.; Colas, P.; Kroemer, G.; Garrido, C. Peptides

DOI: 10.1021/acsnano.8b03726
ACS Nano 2018, 12, 9162−9176

and Aptamers Targeting HSP70: A Novel Approach for Anticancer Chemotherapy. *Cancer Res.* **2011**, *71*, 484−495.
(36) Coles, D. J.; Rolfe, B. E.; Boase, N. R. B.; Veedu, R. N.; Thurecht, K. J. Aptamer-Targeted Hyperbranched Polymers: towards Greater Specificity for Tumours *In Vivo*. *Chem. Commun.* **2013**, *49*, 3836−3838.
(37) Peng, H.; Blakey, I.; Dargaville, B.; Rasoul, F.; Rose, S.; Whittaker, A. K. Synthesis and Evaluation of Partly Fluorinated Block Copolymers as MRI Imaging Agents. *Biomacromolecules* **2009**, *10*, 374−381.
(38) Porsch, C.; Zhang, Y.; Östlund, Å.; Damberg, P.; Ducani, C.; Malmström, E.; Nyström, A. M. *In Vitro* Evaluation of Non-Protein Adsorbing Breast Cancer Theranostics Based on 19F-Polymer Containing Nanoparticles. *Part. Part. Syst. Char.* **2013**, *30*, 381−390.
(39) Carril, M.; Padro, D.; del Pino, P.; Carrillo-Carrion, C.; Gallego, M.; Parak, W. J. *In Situ* Detection of the Protein Corona in Complex Environments. *Nat. Commun.* **2017**, *8*, 1542−5.
(40) Zhang, C.; Peng, H.; Whittaker, A. K. NMR Investigation of Effect of Dissolved Salts on the Thermoresponsive Behavior of Oligo(ethylene glycol)-Methacrylate-Based Polymers. *J. Polym. Sci., Part A: Polym. Chem.* **2014**, *52*, 2375−2385.
(41) Zhang, C.; Peng, H.; Puttick, S.; Reid, J.; Bernardi, S.; Searles, D. J.; Whittaker, A. K. Conformation of Hydrophobically Modified Thermoresponsive Poly(OEGMA-co-TFEA) Across the LCST Revealed by NMR and Molecular Dynamics Studies. *Macromolecules* **2015**, *48*, 3310−3317.
(42) Nylandsted, J.; Rohde, M.; Brand, K.; Bastholm, L.; Elling, F.; Jäättelä, M. Selective Depletion of Heat Shock Protein 70 (Hsp70) Activates A Tumor-Specific Death Program That is Independent of Caspases and Bypasses Bcl-2. *Proc. Natl. Acad. Sci. U. S. A.* **2000**, *97*, 7871−7876.
(43) Pearce, A. K.; Rolfe, B. E.; Russell, P. J.; Tse, B. W. C.; Whittaker, A. K.; Fuchs, A. V.; Thurecht, K. J. Development of A Polymer Theranostic for Prostate Cancer. *Polym. Chem.* **2014**, *5*, 6932−6942.
(44) Truong, N. P.; Zhang, C.; Nguyen, T. A. H.; Anastasaki, A.; Schulze, M. W.; Quinn, J. F.; Whittaker, A. K.; Hawker, C. J.; Whittaker, M. R.; Davis, T. P. Overcoming Surfactant-Induced Morphology Instability of Noncrosslinked Diblock Copolymer Nano-Objects Obtained by RAFT Emulsion Polymerization. *ACS Macro Lett.* **2018**, *7*, 159−165.
(45) Balchin, D.; Hayer-Hartl, M.; Hartl, F. U. *In Vivo* Aspects of Protein Folding and Quality Control. *Science* **2016**, *353*, aac4354.
(46) Dos Santos, T.; Varela, J.; Lynch, I.; Salvati, A.; Dawson, K. A. Effects of Transport Inhibitors on the Cellular Uptake of Carboxylated Polystyrene Nanoparticles in Different Cell Lines. *PLoS One* **2011**, *6*, e24438.
(47) Hinde, E.; Thammasiraphop, K.; Duong, H. T. T.; Yeow, J.; Karagoz, B.; Boyer, C.; Gooding, J. J.; Gaus, K. Pair Correlation Microscopy Reveals the Role of Nanoparticle Shape in Intracellular Transport and Site of Drug Release. *Nat. Nanotechnol.* **2017**, *12*, 81−89.
(48) McKinlay, C. J.; Waymouth, R. M.; Wender, P. A. Cell-Penetrating, Guanidinium-Rich Oligophosphoesters: Effective and Versatile Molecular Transporters for Drug and Probe Delivery. *J. Am. Chem. Soc.* **2016**, *138*, 3510−3517.
(49) Marfori, M.; Mynott, A.; Ellis, J. J.; Mehdi, A. M.; Saunders, N. F. W.; Curmi, P. M.; Forwood, J. K.; Bodén, M.; Kobe, B. Molecular Basis for Specificity of Nuclear Import and Prediction of Nuclear Localization. *Biochim. Biophys. Acta, Mol. Cell Res.* **2011**, *1813*, 1562−1577.
(50) Rodriguez, M. S.; Dargemont, C.; Stutz, F. Nuclear Export of RNA. *Biol. Cell* **2004**, *96*, 639−655.
(51) Jiang, Z.-X.; Liu, X.; Jeong, E.-K.; Yu, Y. B. Symmetry-guided Design and Fluorous Synthesis of A Stable and Rapidly Excreted Imaging Tracer for (19)F MRI. *Angew. Chem., Int. Ed.* **2009**, *48*, 4755−4758.
(52) Longmire, M.; Choyke, P. L.; Kobayashi, H. Clearance Properties of Nano-sized Particles and Molecules as Imaging Agents: Considerations and Caveats. *Nanomedicine* **2008**, *3*, 703−717.
(53) Bose, T.; Latawiec, D.; Mondal, P. P.; Mandal, S. Overview of Nano-Drugs Characteristics for Clinical Application: the Journey from the Entry to the Exit Point. *J. Nanopart. Res.* **2014**, *16*, 2527−2552.
(54) Liu, J.; Yu, M.; Zhou, C.; Zheng, J. Renal Clearable Inorganic Nanoparticles: A New Frontier of Bionanotechnology. *Mater. Mater. Today* **2013**, *16*, 477−486.
(55) Prencipe, G.; Tabakman, S. M.; Welsher, K.; Liu, Z.; Goodwin, A. P.; Zhang, L.; Henry, J.; Dai, H. PEG Branched Polymer for Functionalization of Nanomaterials with Ultralong Blood Circulation. *J. Am. Chem. Soc.* **2009**, *131*, 4783−4787.
(56) Sun, C.-Y.; Shen, S.; Xu, C.-F.; Li, H.-J.; Liu, Y.; Cao, Z.-T.; Yang, X.-Z.; Xia, J.-X.; Wang, J. Tumor Acidity-Sensitive Polymeric Vector for Active Targeted siRNA Delivery. *J. Am. Chem. Soc.* **2015**, *137*, 15217−15224.
(57) Zhang, F.; Zhang, S.; Pollack, S. F.; Li, R.; Gonzalez, A. M.; Fan, J.; Zou, J.; Leininger, S. E.; Pavía-Sanders, A.; Johnson, R.; Nelson, L. D.; Raymond, J. E.; Elsabahy, M.; Hughes, D. M. P.; Lenox, M. W.; Gustafson, T. P.; Wooley, K. L. Improving Paclitaxel Delivery: *In Vitro* and *In Vivo* Characterization of PEGylated Polyphosphoester-Based Nanocarriers. *J. Am. Chem. Soc.* **2015**, *137*, 2056−2066.
(58) Sowers, M. A.; McCombs, J. R.; Wang, Y.; Paletta, J. T.; Morton, S. W.; Dreaden, E. C.; Boska, M. D.; Ottaviani, M. F.; Hammond, P. T.; Rajca, A.; Johnson, J. A. Redox-Responsive Branched-Bottlebrush Polymers for *In Vivo* MRI and Fluorescence Imaging. *Nat. Commun.* **2014**, *5*, 5460.
(59) Meyer, K. L.; Carvlin, M. J.; Mukherji, B.; Sloviter, H. A.; Joseph, P. M. Fluorinated Blood Substitute Retention in the Rat Measured by Fluorine-19 Magnetic Resonance Imaging. *Invest. Radiol.* **1992**, *27*, 620−626.
(60) Lawrence, J.; Lee, S.-H.; Abdilla, A.; Nothling, M. D.; Ren, J. M.; Knight, A. S.; Fleischmann, C.; Li, Y.; Abrams, A. S.; Schmidt, B. V. K. J.; Hawker, M. C.; Connal, L. A.; McGrath, A. J.; Clark, P. G.; Gutekunst, W. R.; Hawker, C. J. A Versatile and Scalable Strategy to Discrete Oligomers. *J. Am. Chem. Soc.* **2016**, *138*, 6306−6310.
(61) Banks, W. A. Characteristics of Compounds That Cross the Blood-Brain Barrier. *BMC Neurol.* **2009**, *9*, S3.
(62) Murphy, M. E. The HSP70 Family and Cancer. *Carcinogenesis* **2013**, *34*, 1181−1188.
(63) Perrault, S. D.; Walkey, C.; Jennings, T.; Fischer, H. C.; Chan, W. C. W. Mediating Tumor Targeting Efficiency of Nanoparticles Through Design. *Nano Lett.* **2009**, *9*, 1909−1915.
(64) Wu, X.; Chen, J.; Wu, M.; Zhao, J. X. Aptamers: Active Targeting Ligands for Cancer Diagnosis and Therapy. *Theranostics* **2015**, *5*, 322−344.
(65) Perrier, S.; Takolpuckdee, P.; Mars, C. A. Reversible Addition−Fragmentation Chain Transfer Polymerization: End Group Modification for Functionalized Polymers and Chain Transfer Agent Recovery. *Macromolecules* **2005**, *38*, 2033−2036.

DOI: 10.1021/acsnano.8b03726
ACS Nano 2018, 12, 9162−9176